# Control of CO2 on flow and reaction paths in olivine-dominated basements: An experimental study

Steve Peuble, Marguerite Godard, Philippe Gouze, Richard Leprovost, Isabelle Martinez, Svetlana Shilobreeva

**Revision 2**

# Control of $CO_2$ on flow and reaction paths in olivine-dominated basements: an experimental study

Steve Peuble[1*], Marguerite Godard[1], Philippe Gouze[1], Richard Leprovost[1], Isabelle Martinez[2] and Svetlana Shilobreeva[3]

[1] *Géosciences Montpellier, Université de Montpellier, CNRS, Place Eugène Bataillon cc060, F-34095 Montpellier Cedex 5, France*

[2] *Institut de Physique du Globe de Paris, Sorbonne Paris Cité, Université Paris-Diderot, UMR 7154 CNRS, 75238 Paris, France*

[3] *Vernadsky Institute of Geochemistry and Analytical Chemistry of Russian Academy of Sciences, Moscow, Russia*

**Corresponding author.*
*Steve Peuble*
Now at : *Mines Saint-Etienne, Univ Lyon, Univ Jean Moulin, Univ Lumière, Univ Jean Monnet, ENTPE, INSA Lyon, ENS Lyon, CNRS, UMR 5600 EVS, UMR 5307 LGF, Centre SPIN, Département PEG, F - 42023 Saint-Etienne, France*
*Email: steve.peuble@mines-stetienne.fr*

## Abstract

The objective of this paper is to quantify the mass transfers involved in the hydrothermal alteration of olivine-rich peridotites in the presence of $CO_2$-enriched waters, and to determine their effects on the rock hydrodynamic properties. Three flow-through experiments were performed at a temperature of 185 °C and a total pressure of 22.5 ± 2.5 MPa. They consisted in injecting a hydrothermal fluid with different concentrations of carbon dioxide ($CO_2$ = 6.26, 62.6 and 659.7 mmol.$L^{-1}$ i.e. $pCO_2$ = 0.1, 1 and 10 MPa, respectively) into cylinders of sintered San Carlos (Arizona, USA) olivine grains. The results show that for low $pCO_2$ conditions (from 0.1 to 1 MPa), olivine is mainly altered into hematite and Mg(Fe)-rich phyllosilicates. Such iddingsitic-type assemblages may clog most of the rock flow paths, resulting in a strong decrease in permeability. Rare Ca-Fe-carbonate minerals also precipitated under these conditions despite the initial Mg-rich system. For higher $pCO_2$ conditions (~10 MPa), olivine is more efficiently altered. A greater amount of poorly crystallized Fe(Mg)-rich phyllosilicates and magnesite is produced, and the carbonation rate of olivine is 3 to 11 times higher than when the $pCO_2$ is 10 to 100 times lower. Interestingly, the changes in porosity caused by the formation of carbonated and hydrous minerals are small while a strong decrease in permeability is measured during the experiments. The formation of reduced carbon is also observed. It is located preferentially at the inlet, where pH is the lowest. This testifies to a competition between reduction (probably associated with the oxidation of ferrous iron) and carbonation; two processes involved in the fixation of $CO_2$ in a mineral form. One may speculate that the formation of reduced carbon can also be a significant mechanism of $CO_2$ sequestration in olivine-dominated basements.



**Keywords:** Olivine, carbonation, reduced carbon, reactive-percolation experiments, porosity, permeability, fluid flow.

## 1. Introduction

Carbonation of mafic and ultramafic rocks (mainly basalts and peridotites) is a widespread process in nature for example, in the past and present oceanic crust and mantle exposed on the seafloor (e.g., Nakamura and Kato, 2004; Ludwig et al., 2006) and within ophiolites (Matter and Kelemen, 2009; Noël et al., 2018). It occurs through the interaction of carbon dioxide ($CO_2$) with divalent metal ions ($Mg^{2+}$, $Fe^{2+}$, $Ca^{2+}$) contained in mafic silicates (e.g., olivine) to precipitate solid carbonate minerals and quartz (e.g., Oelkers et al., 2008):

$$(Mg_{1.80}Fe_{0.20})SiO_4 + 2\ CO_2 = 2\ (Mg_{0.90}Fe_{0.10})CO_3 + SiO_2 \quad (1)$$

*Olivine ($Fo_{90}$)* *Mg-carbonates* *Quartz*

Natural carbonation of mafic and ultramafic basements controls part of the Earth's carbon cycle by contributing to the uptake of $CO_2$ deriving, for example, from the atmosphere, magmatic degassing and C-bearing mineral leaching (Zeebe and Caldeira, 2008; Coggon et al., 2010; Dasgupta and Hirschmann, 2010; Rausch et al., 2013; Kelemen and Manning, 2015). $CO_2$ mineral trapping in mafic and ultramafic aquifers is also envisioned as a safe way for mitigating carbon anthropogenic emissions to the atmosphere (e.g., Seifritz, 1990). This method is being experimented on a large scale via different pilot sites of $CO_2$ injection into basaltic reservoirs (Gislason et al., 2010; McGrail et al., 2011).

In both natural and industrial $CO_2$ geological storage sites, carbon trapping will depend on the mass transfer of solute reactants (products) to (from) reaction interfaces. However, modeling the coupled effects of reactive transport mechanisms during *in situ* mineralization of $CO_2$ in (ultra-)mafic aquifers is challenging because of the complexity of natural systems and the lack of experimental characterization of the effective mechanisms. Most of the laboratory $CO_2$ mineralization experiments are conducted in closed reactors (i.e. with no renewing of the solute) and high water-rock ratios (Pokrovsky and Schott, 2000; Giammar et al., 2005; Hänchen et al., 2006; Hänchen et al., 2008; Daval et al., 2011; Kelemen et al., 2011; Klein and McCollom, 2013; Sissmann et al., 2014). Conversely, aquifers are known to be dynamic systems where local chemical equilibria between fluids and minerals are controlled by low water-rock ratios and pore-scale fluid flow (e.g., Steefel et al., 2005). Extensive outcrops of weathered peridotites show different forms and degrees of $CO_2$ mineralization based on local geological contexts i.e. on small scale variations in the chemistry and hydrodynamic rock properties: carbonates may form large chimneys in deep-sea hydrothermal sites (e.g., Ludwig et al., 2006), travertine deposits from springs in peridotite catchments (Kelemen and Matter, 2008), but also geometrical veins through partially hydrated (Noël et al., 2018) to fully

carbonated peridotites, such as ophicalcite (Bernoulli and Weissert, 1985; Schwarzenbach et al., 2013) and listvenite (Hansen et al., 2005; Nasir et al., 2007).

In agreement with these natural analogues, some recent reactive percolation experiments conducted on ultramafic cores pointed out the role of fluid flow velocity and pore geometry on the nature and rate of carbonation reactions by controlling chemical microenvironments at the pore scale (Andreani et al., 2009; Godard et al., 2013; Peuble et al., 2015a; Peuble et al., 2015b; Luhmann et al., 2017b). Olivine was proposed to be preferentially dissolved in high flow areas facilitating high fluid-rock disequilibrium conditions while carbonates precipitate mostly in reduced flow zones where diffusion-dominated transport favors the mixing of reactants and their high residence time in the vicinity of the reaction zone (Andreani et al., 2009). Similarly, Peuble et al. (2015b) reported that carbonates grow perpendicular to the main fluid flow direction i.e. where the fluid velocity field tends toward zero promoting cationic supersaturation conditions. Chemical microenvironments may vary in space and time within a porous aquifer depending on its structure, flow paths and successive dissolution-precipitation reactions. For instance, the pH of the fluid increases during its percolation in olivine cores leading to changes in secondary mineralogy marked by the replacement of carbonates by serpentine-type minerals (Peuble et al., 2015b). Likewise, a lateral and temporal variation of $CO_2$ concentration may also control fluid-rock interaction reactions. Hänchen et al. (2008) observed that the transformation of olivine into magnesite under a partial pressure of $CO_2$ ($pCO_2$) of 0.1 MPa and a temperature of 120 °C is slowed down by intermediate reactions: it occurs through the destabilization and/or dissolution of hydromagnesite which itself nucleates from brucite. On the other hand, olivine can be directly dissolved into magnesite at a $pCO_2$ of 10 MPa for similar temperature conditions (Hänchen et al., 2008). This would induce significant changes in reaction pathways within mafic and ultramafic reservoirs permeated by $CO_2$ influxes, as $CO_2$ injection wells in the context of C-sequestration industrial sites.

In turn, carbonate formation is likely to have negative feedback effects on fluid flow by decreasing the porosity and permeability of the rock (Oelkers et al., 2008; Jun et al., 2013; Peuble et al., 2015b). The alteration of olivine-dominated basements into carbonates is considered as a volume-increasing process since the volumetric mass density of products (e.g., 3.0 $g.cm^{-3}$ for magnesite) is lower than that of reactants (e.g., 3.3 $g.cm^{-3}$ for olivine) (Deer et al., 1992). As a result, the further carbonation of mafic silicates will rely on cracks, induced by tectonic stresses (Andreani et al., 2007) or by crystal-growth (Jamtveit et al., 2008; Rudge et al., 2010; Kelemen and Hirth, 2012), to preserve fluid pathways in the host

rock unless reaction products are leached out by the fluid flow to maintain pore volume and permeability at reaction interfaces (Godard et al., 2013; Peuble et al., 2017).

Defining the main parameters controlling the development of one suite of chemical and mineralogical reactions at the expense of another, but also their feedback effects on hydrodynamic rock properties is therefore challenging in systems as complex as natural geological porous media where temperature, pressure, composition and permeability will change along flow paths. Numerical simulations allow to integrate the role of coupling between chemistry, transport and fluid flow e.g., JChess geochemical code (Van der Lee et al., 2003) or PhreeqC geochemical code (Parkhurst and Appelo, 2013). However, these modelling tools are designed to handle transport at the Darcy's scale for which the primary upscaling of the flow and transport is implicitly performed. This implies that the local spatial variability of the velocity field (controlled by the Stokes flow) inherent to the geometrical heterogeneity of the connected porosity as well as the local mineralogical heterogeneity are averaged into volumes, named as Representative Elementary Volumes (REV) encompassing several pores. For instance, these models assume (*i*) a full mixing of solutes at the REV scale and comprehensibly a full accessibility of all reactants to reactive surfaces, and (*ii*) a constant residence time of chemical species into the entire REV. The results of the flow-through experiments cited above indicate clearly that these assumptions cannot be considered a priori, i.e. that pore scale heterogeneities are often controlling overall mass transfers for the space and time characteristics under consideration. Yet, the scarcity of experimental data compared to the large variability of potentially realistic situations makes the derivation of reliable upscaling models challenging. For example, it is critical to study the functional dependencies between chemical, hydrodynamic and mechanical processes for experimental configurations with low degree of freedom, in order to characterize the role of surface processes and kinetics versus equilibrium (Pokrovsky and Schott, 2000; Bearat et al., 2006; Daval et al., 2013).

In this paper, we present and discuss the results of three reactive percolation experiments conducted on sintered olivine cores at various $CO_2$ partial pressure ($pCO_2$). All other characteristics are similar for the three experiments. The objective of this study is to investigate olivine alteration processes under different $pCO_2$ in order to reproduce the conditions close and far from a $CO_2$ inflow percolating an ultramafic setting. We aim to characterize the mechanisms controlling fluid chemistry, secondary mineralogy and their consequences on the hydrodynamic rock properties (i.e. porosity and permeability) in the context of $CO_2$-fluids interactions with ultramafic rocks. Results are compared to previous

experimental studies and discussed in the context of natural and anthropically induced hydrothermal systems in ultramafic rocks.

## 2. Methodology

### *2.1. Experimental protocol*

Three reactive percolation experiments were performed using the Icare Lab 3 reactive flow-through system (ICARE-RFTS3, Geosciences Montpellier). They were conducted under similar conditions of flow injection rate (0.5 $mL.h^{-1}$), temperature (185 °C) and average pressure (22.5 ± 2.5 MPa), but with setting the $pCO_2$ of the injected fluid at 0.1, 1 and 10 MPa respectively in order to investigate only the effect of changes in $CO_2$ concentration on fluid-rock interactions.

The ICARE-RFTS3 experimental device allows the injection of solutes through permeable samples over the range of pressure and temperature conditions expected in hydrothermal systems and in geological reservoirs targeted for $CO_2$ sequestration: $P$ = 0.5 – 40 MPa and $T$ = 50 – 400 °C. It is built for exploring mass transfer processes from kinetic-controlled to transport-controlled conditions for samples displaying permeability values ranging from $10^{-20}$ to $10^{-13}$ $m^2$.

ICARE-RFTS3 (Fig. 1) includes (*i*) a fluid injection system, comprising three computer-controlled motorized dual-piston pumps programmed to achieve the mixing of $CO_2$ with water and then inject the mixture through the sample at a constant flow rate, (*ii*) a heated sample-holder, maintaining the sample at the given confinement pressure using a motorized piston pump, (*iii*) a back pressure controller equipment, composed of a motorized piston pump coupled with a large volume pneumatic dumper, and (*iv*) an automatic sampling system, allowing to sample ≈ 3 mL of fluid directly from the rock sample outlet. All surfaces of the ICARE-RFTS3 system in contact with the fluid are made of Hastelloy C22. The motorized piston pumps are equipped with displacement encoders allowing an accurate control of the flow injection rate; fluctuations are less than 0.1% of the flow injection rate. Continuous flow rates ranging from $3.4 \times 10^{-3}$ to $10^2$ $mL.h^{-1}$ ($9.5 \times 10^{-13}$ – $2.8 \times 10^{-8}$ $m^3.s^{-1}$) can be operated. All pumps, valves and the sampling system are controlled by a LabView® program according to the user requirements. Both axial and radial confining pressures are applied to the sample fitted into a tight Teflon sleeve. The confinement pressure is set to 112% of the inlet fluid pressure during the experiments (from the loading to the unloading of the circuit fluid

pressure) in order to minimize deviatoric stresses. During reactive percolation experiments, a porous nickel sinter is positioned upstream of the sample to ensure a homogeneous distribution of the flow.

The difference in fluid pressure between the inlet and the outlet of the sample, $\Delta P$ (in Pa), is monitored during the experiments using a differential pressure sensor (Rosemount® 3051 with an accuracy of $3 \times 10^3$ Pa) coupled with two high-resolution pressure sensors (Keller® PA-33x with an accuracy of $3.5 \times 10^4$ Pa). Assuming laminar flow conditions, the sample permeability $k$ (in m²) was calculated from Darcy's law:

$$\boldsymbol{k} = \frac{\boldsymbol{Q}.\mu.\boldsymbol{L}}{\boldsymbol{S}.\Delta\boldsymbol{P}} \quad (2)$$

where $Q$ is the flow injection rate ($m^3.s^{-1}$), $L$ and $S$ the length (m) and section area (m²) of the sample, respectively, and $\mu$ is the dynamic fluid viscosity set at $1.5 \times 10^{-4}$ Pa.s for water at 185 °C (Mao and Duan, 2009).

*2.2. Preparation and composition of olivine cores and injected fluids*

The percolation experiments were performed on cores (≈ 16 mm length × 6.35 mm diameter) made of sintered San Carlos (Arizona, USA) olivine grains. The sintering technique was used because it allows obtaining solid aggregates of controlled porosity and composition (Table 1 and Appendix A1).

The starting material consisted of millimeter-size grains of San Carlos olivine ($Fo_{90}$, see Appendix A1). Olivine grains were sorted under binocular microscope to eliminate those having spinels or pyroxenes on their surfaces or as inclusions. The selected grains were crushed and sieved. The 100 – 150 µm olivine fraction was then cleaned ultrasonically for 10 min in diluted hydrochloric acid (≈ 2% HCl) to remove any carbonate grains and finally rinsed in MilliQ-water for 15 min. The cleaning and rinsing procedure was repeated three times before drying the powder at 110 °C for 12 hours. Bulk composition of the resulting olivine powder was analyzed by X-ray fluorescence spectroscopy (Geolabs, Canada) and compared to the composition of the olivine grains measured by electron probe micro-analyzer (EPMA, University of Montpellier; Appendix A1). Bulk and mineral compositions were similar indicating that no contamination occurred during the preparation procedure.

Three sintered olivine cores were made using the following procedure. First, the 100 – 150 µm fraction of the cleaned olivine powder was pressed at 5 MPa and 25 °C in stainless steel capsules. Then, samples were sintered at a temperature of 1180 °C and a confining

pressure of 150 MPa using a gas medium (Ar) high-pressure and high-temperature vessel (Paterson, 1990) at Geosciences Montpellier. For each core, the initial porosity was measured before the percolation experiment using the triple weight method (Dullien, 1979); it ranged between 10.57 and 11.30 ± 0.10% (Table 1). Experiments were performed on samples named SC1-L, SC2-M and SC3-H, which have similar initial permeability ($1.6 – 4.6 \times 10^{-15}$ $m^2$; Table 1).

The inlet fluid was a mineral water (Volvic®) mixed with various concentrations of gaseous $CO_2$. The Volvic® water was selected because of its chemical composition that is stable and typical of aquifers containing mafic minerals (e.g., olivine) under low temperature conditions (50 – 200 °C; Table 2 and Appendix A2). The rationale was to reproduce chemical conditions similar to those anticipated for $CO_2$ industrial storage in igneous basements, close and far from an injection site. The Volvic® water was first vacuumed for three hours at room temperature to degas it and thus reproduce anoxic conditions. Then it was mixed with gaseous $CO_2$ at 30 MPa and 25 °C by repeated back-and-forth pumping between two out of the three injection pumps for three hours (Fig. 1). The pH of Volvic® water at 25 °C is 7.0. After mixing with $CO_2$, the inlet fluid pH at 185 °C and 22.5 ± 2.5 MPa was calculated using PhreeqC and the Lawrence Livermore National Laboratory 'thermo.com.V8.R6.230' thermodynamic database (Parkhurst and Appelo, 2013): pH = 4.5, 3.9 and 3.4 for the experiments SC1-L (experiment at the lowest $pCO_2$ = 0.1 MPa; $CO_2$ = 6.26 $mmol.L^{-1}$), SC2-M (experiment at medium $pCO_2$ = 1 MPa; $CO_2$ = 62.6 $mmol.L^{-1}$) and SC3-H (experiment at the highest $pCO_2$ = 10 MPa; $CO_2$ = 659.7 $mmol.L^{-1}$), respectively.

### *2.3. Analytical methods*

The chemical composition of the inlet and outlet fluids was measured on an Agilent 7700x inductively coupled plasma – mass spectrometer (ICP–MS) at Geosciences Montpellier (AETE platform, France). All fluids were previously diluted by two in an acidified MilliQ-water (≈ 2% of nitric acid). Indium (1 ppb) was used as an internal standard during analyses. Both accuracy and reproducibility of the measurements were assessed with the SLRS-5 water standard. The analytical results were within the range of compiled values (Yeghicheyan et al., 2013). The external reproducibility was better than 5% for all measured elements. The Si, Mg, Fe and Ca concentrations of the inlet and outlet fluids and of the SLRS-5 water standard are reported in Table 2 and in the Supplementary Materials (Appendix A3).

Both composition and mineralogy of the reacted aggregates were characterized with the methodology described thereafter. Samples magnetic susceptibility was measured before and after each experiment on a Bartington–MS2 meter susceptibility system operating at 0.565 kHz for values ranging from $1 \times 10^{-8}$ to $9999 \times 10^{-8}$ $m^3.Kg^{-1}$ with an uncertainty of ≈ 1% (Geosciences Montpellier).

After magnetic susceptibility measurements, the reacted cores were longitudinally sawn into two semi-cylindrical halves. The first half was polished for microscopic and spectroscopic characterizations (scanning electron microscopy, Raman spectroscopy and electron probe micro-analyzer) according to the protocol described in detail in Peuble et al. (2015a). The second half was crushed for bulk powder analyses (Mössbauer spectroscopy and bulk rock carbon and hydrogen measurements).

Polished sections were described optically, then backscattered (BSE) and secondary electron (SE) images were collected on a FEI Quanta FEG 200 scanning electron microscope (SEM) using an acceleration voltage of 15 kV and an ambient pressure of 0.45 torr (University of Montpellier, France).

Secondary minerals have been also identified on LabRam Aramis IR2 (Charles Gerhardt Institute, Montpellier, France) and XploRa (Laboratory of Geology of Lyon, France) confocal Raman spectrometers (Jobin-Yvon SA, Horiba, France); both equipped with a charge-coupled device (CCD) detector. Raman analyses were performed with 473 nm (LabRam Aramis IR2) and 532 nm (XploRa) radiations from diode lasers generating less than 1 mW. The spectra resolution is ± 2 $cm^{-1}$. Before analyses, Raman spectrometers were calibrated using a crystalline silicon thin-section showing a large band at 521 ± 2 $cm^{-1}$.

The composition of primary and secondary minerals was measured on carbon-coated polished sections (thus precluding further investigations on C-phases) using a Cameca SX-100 EPMA (University of Montpellier) equipped with five wavelength-dispersive X-ray spectrometers (WDS). Analyses were done at an acceleration potential of 20 kV and a beam current of 10 nA. Results are summarized in Appendix A1.

The presence (or lack) of ferric iron in the reacted samples was measured by Mössbauer spectroscopy at the Charles Gerhardt Institute (Montpellier, France) with a detection limit of ≈ 2%. Mössbauer data were acquired at ambient temperature on ≈ 200 mg bulk rock powders in the constant acceleration mode. $^{57}Fe$ Mössbauer spectra were obtained using a source of $^{57}Co$ in rhodium metal. The spectrometer was operated using a triangular velocity waveform. Gamma rays were detected with a NaI scintillation detector. Spectra were fitted with a combination of Lorentzian lines then used to determine the spectral parameters i.e. the isomer

shift (IS), the electric quadrupole splitting (QS), the full line width at half maximum (LW) and the relative resonance areas (A) of different components of the absorption patterns (see Appendix A4). The magnetic hyperfine field (H) is absent in the case of these samples confirming the paramagnetic character of the analyzed phases.

Bulk carbon (in inorganic and organic form) and water compositions were determined using step-heating experiments (Javoy and Pineau, 1991; Pineau and Javoy, 1994) at the IPGP (Institut de Physique du Globe de Paris, France) on ≈ 100 mg aliquots. First, powders were loaded in a quartz tube connected to a vacuum line and degassed one night at room temperature. A vertical cylindrical furnace (with a temperature stability of ± 2 °C) was then used to heat progressively the samples at 100 °C for 1 hour to eliminate all surface contaminants e.g., water and other adsorbed compounds. Finally, samples were heated 1 hour at 700 °C and 1 hour at 1100 °C to extract the carbon trapped in the organic and inorganic form respectively. Heating was made under an oxygen atmosphere raised up to 0.4 MPa after 30 min of reaction. Liquid nitrogen was used to cryogenically separate and collect gaseous $CO_2$ and $H_2O$. The amount of $CO_2$ was quantified using a Toepler® pressure gauge with a detection limit of 0.05%. Carbon and water analyses were duplicated to ensure the reproducibility of the data.

## 3. Results

### *3.1. Permeability*

All reactive percolation experiments displayed a reduction in sample permeability from initial values of 1.6 – 4.6 × $10^{-15}$ m² (Table 1) down to 0.075 × $10^{-15}$ m² (SC1-L), 0.019 × $10^{-15}$ m² (SC2-M) and 0.005 × $10^{-15}$ m² (SC3-H; Fig. 2). In detail, the way in which permeability decreased varied from one experiment to the other.

The permeability of experiment SC1-L decreased slightly in the early hours of injection ($dk/dt$ = 1.40 × $10^{-17}$ m².h$^{-1}$) before dropping down to 0.08 × $10^{-15}$ m² at $t$ ≈ 36h and declining slightly again until the end of fluid injection ($dk/dt$ = 6.30 × $10^{-19}$ m².h$^{-1}$).

Experiment SC2-M is characterized by four periods of fast permeability drop starting at $t$ ≈ 13h ($dk/dt$ = 1.40 × $10^{-15}$ m².h$^{-1}$), $t$ ≈ 54h ($dk/dt$ = 5.62 × $10^{-16}$ m².h$^{-1}$), $t$ ≈ 84h ($dk/dt$ = 9.29 × $10^{-17}$ m².h$^{-1}$) and $t$ ≈ 107h ($dk/dt$ = 2.10 × $10^{-16}$ m².h$^{-1}$). These periods were separated by four intervals of low permeability decrease of about 13, 41, 30 and 23 hours, respectively.

The permeability of experiment SC3-H is marked by a slow and almost constant decrease of 135 hours ($dk/dt = 1.5 \times 10^{-17}$ m².h$^{-1}$), then accelerating sharply at $dk/dt = 4.3 \times 10^{-17}$ m².h$^{-1}$. After 168 hours, the decrease in permeability slowed down to $dk/dt = 1.4 \times 10^{-18}$ m².h$^{-1}$ until the end of injection.

*3.2. Fluid chemistry*

The outlet fluids composition at the time of sampling (Fig. 3) denotes the value integrated over the volume of fluids having flowed and reacted with the olivine cores over the 6 hours of reactive percolation experiments preceding sampling (each fluid sample is 3 mL and fluid flux $Q$ is 0.5 mL.h$^{-1}$). The three experiments were marked by significant changes with time in the outlet fluids composition compared to the injected $CO_2$-water. First, all outlet fluids displayed enrichments in the three major components of olivine (i.e. Si, Mg and Fe; Fig. 3a,b,c) testifying to the dissolution of the Mg-silicate during the experiments. Second, the sampled outlet fluids were (or became) depleted in Ca indicating the trapping of this element in the percolated cores through the precipitation of Ca-bearing mineral(s) (Fig. 3d). However, the amount of cations released or trapped per time unit varied between the experiments. It should be noted that the outlet fluids sampled at the earliest stages of all experiments (time of sampling < 20h) systematically displayed chemical compositions at odds with the overall chemical trends showed later in the experiments. These variations are controlled by the dissolution of a minor fraction of small grains produced during the preparation of olivine aggregates (Andreani et al., 2009; Godard et al., 2013; Peuble et al., 2015b). These initial processes will not be discussed in details thereafter and we will mainly focus our analysis to $t$ > 20h.

Experiment SC1-L (lowest concentration in $CO_2$ = 6.26 mmol.L$^{-1}$) showed a slight increase in the outlet concentrations of Si (from 43.7 to 62.0 ppm), Mg (from 13.5 to 14.8 ppm) and Fe (from 0.2 to 0.7 ppm). But the amount of Mg and Fe is low compared to that of Si and to the olivine stoichiometry; the molar ratios of $(Mg/Si)_{(outlet\text{-}inlet)}$ and $(Fe/Si)_{(outlet\text{-}inlet)}$ in sampled fluids are 0.15 and 0.01, respectively. This indicates either that the dissolution of olivine was non-stoichiometric or, more probably, that some of the Mg and Fe released upon olivine dissolution remained trapped in the percolated core. The concentrations of Ca, brought in by the inlet fluid, decreased with time from 12.6 to 10.8 ppm in the sampled fluids. This decrease, particularly marked in the first 48 hours of injection (Fig. 3d), suggests that the outlet fluids Ca composition is partly controlled by cation trapping mechanisms. It is worth

noting that the change in chemistry observed in the outlet fluids after 48 hours is close in time to the change in permeability recorded in experiment SC1-L at $t \approx 36$h.

During experiment SC2-M (medium concentration in $CO_2$ = 62.6 mmol.L$^{-1}$), Si, Mg and Fe also displayed an increase in their outlet concentrations with time. However, Si concentrations were high (107 to 261 ppm) and their variations erratic (peaks observed at $t \approx$ 13, 83, 134 and 147 hours; Figure 3a) compared to experiment SC1-L. Mg concentrations increased steadily during about 48 hours before stabilizing around 25 ppm. The increase in Fe concentrations followed two plateaus, the first at ≈ 0.3 ppm (from 13 to 109 hours) and the second at ≈ 0.5 ppm (after 122 hours). Compared to experiment SC1-L, Ca concentration values in experiment SC2-M were overall low, decreasing from 12.2 to 9.1 ppm over time. Chemical trends of Si, Mg, Fe and Ca were interpreted as indicating both dissolution of olivine and trapping of Mg, Fe and Ca in the percolated core. Molar ratios of $(Mg/Si)_{(outlet\text{-}inlet)}$ and $(Fe/Si)_{(outlet\text{-}inlet)}$ were low compared to experiment SC1-L with values of 0.09 and 0.002, respectively; suggesting that the mechanisms controlling the trapping of Mg and Fe were overall more efficient in experiment SC2-M. The irregular and abrupt changes in fluid chemistry during experiment SC2-M also suggest that complex feedback processes between these trapping mechanisms, olivine dissolution and fluid fluxes occurred. For instance, the increase in Mg relative to Si in the first 48 hours suggests that Mg-trapping became less efficient than olivine dissolution yet this period is associated to a strong permeability drop. After 122 hours, the experiment is marked by an increase in Si, Fe and, to a lesser extent, in Ca revealing a further decrease in trapping efficiency while olivine dissolution continued and permeability remained stable.

Compared with experiments SC1-L and SC2-M, the outlet fluids sampled in experiment SC3-H (highest concentration in $CO_2$ = 659.7 mmol.L$^{-1}$) are depleted in Fe, but enriched in Mg compared to experiments SC1-L and SC2-M, and in Si compared to experiment SC1-L. Fluid time series are also distinguished by contrasting chemical variations defining two time periods (Fig. 3). The first period, from the start to $t \approx$ 144h, is characterized by large changes in the concentrations of all elements: Si concentrations increased rapidly then stabilized at ≈ 82 ppm at $t \approx$ 38h; Mg concentrations increased sharply at the beginning then slower after ≈ 38h before reaching a peak at 64.1 ppm (at $t \approx$ 70h) and decreasing down to 38.3 ppm; Fe concentrations were strongly depleted (< 0.03 ppm) except for a peak (up to 0.19 ppm) between 96 and 140 hours; Ca concentrations showed a strong increase during the first hours until a peak (10.5 ppm) was reached at $t \approx$ 45h followed by a decrease down to 4.7 ppm (at $t \approx$ 135h). In contrast, the second period, starting after $t \approx$ 144h, is characterized by little to no

variations in fluid chemistry. Only Si showed a slow increase up to ≈ 106 ppm and Mg displayed a slight increase at ≈ 45 ppm after 216 hours. Molar ratios of $(Mg/Si)_{(outlet-inlet)}$ and $(Fe/Si)_{(outlet-inlet)}$ were low in the SC3-H sampled fluids (0.54 and 0.0005, respectively) suggesting an efficient trapping of Mg and Fe in the olivine aggregate. However, in contrast to the low $pCO_2$ experiments, $(Mg/Si)_{(outlet-inlet)}$ changed significantly from 0.70 to 0.43 after $t$ ≈ 144h indicating either a higher release of Si relative to Mg during the dissolution of olivine and/or a more efficient trapping of Mg (together with Ca) during the second period of experiment SC3-H. These chemical changes are associated to variations in rock hydrodynamic properties; the first period is characterized by slow changes in permeability while a significant drop in permeability marks the second period.

### *3.3. Characterization of the reacted samples*

Optical observations shows that the three rock samples remained mainly composed of olivine after the percolation experiments. However, the initial green olivine crystals are covered by a red hue decreasing in intensity away from the inlet (Fig. 4). The red hue coating increases with the $CO_2$ partial pressure value used in the experiment; it extends to few mm² in sample SC1-L, three-quarters of sample length for sample SC2-M and the whole sample for sample SC3-H.

At the micrometric scale, SEM analyses allow the identification of secondary minerals in the three percolated cores (Fig. 5 and Appendix A1). For the lowest $pCO_2$ experiments (SC1-L, SC2-M), some pores contain clusters of an amorphous phyllosilicate enriched in Mg ± Fe (Fig. 5a and Appendix A1). Raman analyses suggest that this phase may represent a poorly crystallized precursor of Mg-Fe-rich hydrous minerals such as Fe(III)-rich serpentine (Fig. 6), which is commonly observed in the earliest stages of serpentinization (Andreani et al., 2013). It has Raman peaks comparable to those of lizardite, with a band at 1104 $cm^{-1}$ (Auzende et al., 2004), and those of iddingsite, a Fe(III)-rich olivine alteration product having a non-definite crystal structure, with a first band observed between 611 and 663 $cm^{-1}$ and a second in the O-H bonds spectral region from 3500 to 3600 $cm^{-1}$ (Kuebler, 2013). This alteration product is probably localized at the surface of olivine grains, since olivine peaks are also identified on the Raman spectrum at 824 and 857 $cm^{-1}$ (Cnopnras, 1991). It is associated with hematite showing four Raman bands at 224, 300, 411 and 1322 $cm^{-1}$ (De Faria et al., 1997). Both hydrous phases and iron oxides are found preferentially along the olivine rims located in the vicinity of the inlet; they account for the red hue covering the reacted samples (Fig. 4).

Samples SC1-L and SC2-M contain also micro-grains of silica, Mg-Fe-bearing calcite ($Ca_{0.95}Mg_{0.03}Fe_{0.02}CO_3$) and minor siderite ($Fe_{0.95}Mg_{0.04}Ca_{0.01}CO_3$) that are distributed evenly along the percolated cores (Fig. 5b-c and Appendix A1).

In sample SC3-H, some olivine surfaces exhibit dissolution features forming conical-shaped etch-pits with a maximum length of 1 µm (Fig. 5d-e). Etch-pits are observed along the dissolved olivine surfaces in large pores (10-50 µm) and within the micro-fissures (< 5 µm) that were probably induced by the sample preparation (Peuble et al., 2015a). Sample SC3-H also displays large Mg-carbonate crystals ($Mg_{0.91}Ca_{0.07}Fe_{0.02}CO_3$) forming a matrix of several tens of µm in the pores (Fig. 5f and Appendix A1). This carbonate was identified as magnesite with the typical Raman peak of C-O bonds observed at 1094 $cm^{-1}$ and three minor peaks at 209, 325 and 738 $cm^{-1}$ (Rividi et al., 2010 – see Figure 9). In addition to magnesite, a poorly crystallized phyllosilicate enriched in Fe ± Mg was also characterized in sample SC3-H (Fig. 5d and Appendix A1). This phase forms a dense network of curled fibers similar to the proto-serpentine observed in previous flow-through experiments (Godard et al., 2013). Its Raman spectrum is comparable to the poorly crystallized phase identified in samples SC1-L and SC2-M, forming an assemblage of hydrous minerals and hematite at the olivine grains surface (Fig. 6). The attenuation of the Raman peaks of olivine compared to this proto-serpentine precursor suggests a greater degree of crystallization of the latter in experiment SC3-H than in experiments SC1-L and SC2-M (Kuebler, 2009).

Black grains were observed in pores located close to the inlet in the three reacted samples (< 5 mm - see Figs. 4 and 8). These micron-size grains (<20 µm) were identified as carbon from the D and G bands observed at respective values of 1310 and 1520 $cm^{-1}$ on Raman spectra (e.g., Galvez et al., 2013). Carbon grains have a symmetrical G band in Raman analyses indicative of a poorly ordered crystallographic structure also referred to as turbostratic. Reduced turbostratic carbon or graphene is commonly reported under low temperature conditions i.e. < 400 °C (Audier et al., 1981; Beyssac et al., 2003).

Magnetic susceptibility and Mössbauer analyses were realized on a subset of powders. They show that the precipitation of ferric iron is minimal in the three reacted cores in spite of the change of color observed optically. Samples magnetic susceptibility did not change significantly during reactive percolation experiments suggesting that magnetite did not precipitate during $CO_2$-fluids injection (see Table 1). Mössbauer measurements identified no ferric iron impurities in the reacted powders in the limit of ≈ 2% (see Fig. 9 and Appendix A4). Note that all Mössbauer spectra were fitted using two doublets (components 1 and 2 corresponding to the M1 and M2 sites of olivine), both having the parameters of high spin

475 $Fe^{2+}$ occupying octahedral sites in the olivine crystals. The isomer shifts and the quadrupole
476 splitting are similar to the reported values for olivine (Dyar et al., 2006). The only differences
477 between these samples are the line widths and the relative fractions of components 1 and 2,
478 which are both within the uncertainty of Mössbauer analyses (i.e. less than ≈ 2% relative to
479 the total iron content).
480 Bulk rock hydrogen and carbon analyses indicate that reacted samples were systematically
481 enriched in these two elements relative to the initial olivine (Table 3 and Appendix A5). This
482 is consistent with the presence of secondary hydrous and carbon-bearing phases revealed by
483 the petrological and mineralogical analyses of reacted samples. Bulk powder measurements
484 also show that carbon is present in both inorganic and organic forms in reacted samples SC2-
485 M and SC3-H. Inorganic carbon (carbonates) is dominant after the highest $pCO_2$ experiment:
486 it represents 97% of the total carbon measured in sample SC3-H. In contrast, inorganic carbon
487 represents only ~ 40% of the measured total carbon in sample SC2-M; the remaining fraction
488 being organic (i.e. reduced) carbon, which suggests less favorable conditions for carbonates
489 precipitation under a lower $pCO_2$.
490
491 *3.4 Mass estimates of dissolved and precipitated minerals*
492
493 Both olivine and secondary minerals are mainly composed of Si, Mg, Fe and Ca. The
494 mass balance calculation (expressed as oxides mass) of these cations comparing inlet and
495 outlet fluids provides a first insight of the volatile-free bulk mass lost or gained by the
496 ultramafic cores during the experiments (Peuble et al., 2015b). Calculations indicate a total
497 mass loss of 0.22, 1.60 and 2.39% relative to the initial samples mass in experiments SC1-L,
498 SC2-M and SC3-H, respectively (Appendix A6), even though the Ca brought in by fluids is
499 trapped into the samples.
500 Hydrous minerals, oxides and carbonates were identified as secondary phases in the
501 percolated aggregates. Some identified minerals display unreferenced compositions (such as
502 the hydrous phases interpreted as serpentine precursors), albeit they all contain at least Si, Mg,
503 Fe or Ca. Furthermore, bulk analyses could not be used directly to quantify the amount of
504 carbon and hydrogen trapped in reacted samples. First, due to technical problems, hydrogen
505 was not analyzed in one of the samples (sample SC3-H). Second, the distribution of hydrogen
506 and organic and inorganic carbon in sample SC1-L may have been affected by leakage of
507 containment fluid (MilliQ-water in equilibrium with the atmosphere) into the sample Teflon
508 sleeve, when the experiment was stopped ($t$ ≈ 93h). For these reasons, the quantification of

dissolved and trapped phases was done only on the basis of fluid time series. In such conditions, estimating the actual mass change of the samples during reactions requires making conjectures on the distribution of cations in secondary minerals (Andreani et al., 2009). For this study, we assume that:

(*i*) The excess of Si measured in the outlet fluids, i.e. $Si_{(outlet-inlet)}$, equals to the Si released by the dissolution of olivine only. In other words, we assumed that the amount of Si trapped in the samples is negligible even if Si-rich secondary phases precipitated in the reacted cores. The calculated mass of dissolved olivine is thus a minimal estimate. Accordingly, we calculated a concentration model of the outlet fluids for Mg and Fe involving the mass of these elements released by olivine dissolution and the mass brought in by the injected fluid. The measured deficits in Mg and Fe relative to this concentration model allow estimating the mass of trapped minerals.

(*ii*) Fe was trapped in carbonates during experiments SC1-L and SC2-M, and Mg was sequestered as magnesite in experiment SC3-H. All Ca was incorporated into carbonates in the three experiments (Fe-bearing calcite in samples SC1-L and SC2-M; Ca-bearing magnesite in sample SC3-H).

(*iii*) The contribution of hydrous silicate minerals associated to (proto-)serpentinization of olivine was approximated from pure end-member components that have been described as 'precursor phases' of serpentine minerals: brucite ($Mg(OH)_2$) for the Mg(Fe)-rich phyllosilicates in experiments SC1-L and SC2-M (e.g., Ferry, 2000; Tutolo et al., 2018); goethite (FeO(OH)) for the Fe(Mg)-rich phyllosilicates in experiment SC3-H (Delvigne et al., 1979; Lee et al., 2015).

The calculated mass of dissolved olivine is 8.34, 63.17 and 62.94 mg in experiments SC1-L, SC2-M and SC3-H, respectively. This represents a mass loss of 0.48, 3.69 and 4.31% relative to the initial mass of samples SC1-L, SC2-M and SC3-H, respectively (Table 4 and Fig. 10). The calculated mass of hydrous Mg-phases in samples SC1-L and SC2-M is 6.82 and 54.08 mg, respectively; this indicates a gain of mass of 0.40 and 3.15% relative to their initial mass, respectively. The calculated mass of hydrous Fe-phases in sample SC3-H is 7.28 mg, corresponding to a relative mass gain of 0.50%. The total mass of carbonates is 1.30, 9.98 and 45.60 mg in samples SC1-L, SC2-M and SC3-H, respectively, representing a relative mass gain of 0.08, 0.58 and 3.12%.

Petrological observations and bulk rock analyses indicated that organic carbon was present in the reacted samples. Bulk rock analyses showed that the carbon content of the initial olivine was below the detection limit, so the only source of carbon is the $CO_2$-bearing

injected fluid. In order to evaluate the amount of organic carbon in the three reacted samples, we assumed that (*i*) the measured ratios of organic and inorganic carbon for samples SC3-H and SC2-M were representative of the actual distribution of carbonates versus reduced carbon in the samples, and (*ii*) the ratio of organic and inorganic carbon in sample SC1-L was the same as that of sample SC2-M. Based on the calculated masses of carbonates, the total mass of reduced carbon is 0.19, 1.77 and 0.20 mg in samples SC1-L, SC2-M and SC3-H, respectively and corresponds to a relative mass gain of 0.01, 0.10 and 0.01%, respectively.

Based on these calculations, the mass balance between dissolved olivine and precipitated secondary minerals (hydrous phases, reduced carbon and carbonates) led to a negligible total mass change of the cores: a relative mass gain of 0.01 and 0.14% for samples SC1-L and SC2-M, respectively, and a relative mass loss of 0.68% for sample SC3-H. They also indicate that the alteration of olivine into carbon-bearing phases (reduced carbon and carbonates) resulted in a total sequestration of $CO_2$ of 0.07, 0.60 and 1.66 wt.% in experiments SC1-L, SC2-M and SC3-H, respectively (see Table 4). These values are consistent with bulk rock data measured of samples SC2-M and SC3-H (Fig. 10), which validates a posteriori the assumptions made for the mass balance. Calculations also showed that only 10.5, 4.8 and 0.5% of the total amount of $CO_2$ injected in samples SC1-L, SC2-M and SC3-H respectively, remained trapped as carbon–bearing products (reduced carbon and carbonates). This implies that the percolating fluids were still enriched in $CO_2$ at the cores outlet.

### *3.5. Porosity variation during olivine alteration*

Changes in rock porosity induced by the percolation of $CO_2$-fluids in the ultramafic cores can be inferred from the calculated mineral masses. A volumetric mass density of 3.3 g.cm$^{-3}$ was assumed for olivine (Deer et al., 1992). The total volume of carbonates was assessed from the volumetric mass density of calcite ($\rho_{calcite}$ = 2.7 g.cm$^{-3}$) and siderite ($\rho_{siderite}$ = 3.9 g.cm$^{-3}$) in experiments SC1-L and SC2-M, and of magnesite ($\rho_{magnesite}$ = 3.0 g.cm$^{-3}$) in experiment SC3-H (Deer et al., 1992). Two end-member scenarios were used to estimate the volume of hydrous phases considering the density of their expected precursors (brucite in samples SC1-L and SC2-M ($\rho_{brucite}$ = 2.4 g.cm$^{-3}$); goethite in sample SC3-H ($\rho_{goethite}$ = 4.3 g.cm$^{-3}$)) or that of lizardite as a serpentine-type mineral ($\rho_{lizardite}$ = 2.6 g.cm$^{-3}$) (Deer et al., 1992). The precipitation of reduced carbon was considered as negligible.

Results show that changes in porosity are relatively small during the percolation experiments (Table 4, Fig. 10c and Appendix A7). Samples porosity was reduced from 10.96% to 10.80% in experiment SC1-L and from 11.30% to 9.89% in experiment SC2-M according to the different scenarios of carbonate formation (calcite or siderite) and hydration (brucite or lizardite). Compared to the initial samples porosity, these results correspond to a maximum porosity change of ~1% and ~12% in experiments SC1-L and SC2-M, respectively. In experiment SC3-H, the porosity increased by ~5% (from 10.57 to 11.11%) or ~3% (from 10.57 to 10.86%) considering the precipitation of magnesite and goethite or the precipitation of magnesite and lizardite, respectively.

## 4. Discussion

All reacted samples show the alteration of olivine into secondary minerals. However, the nature and rate of dissolution and precipitation reactions are variable depending on the inlet fluid $pCO_2$. The experiments with the lowest $pCO_2$ (0.1 – 1 MPa i.e. $CO_2$ = 6.26 – 62.6 mmol.$L^{-1}$) are characterized by the formation of Mg(Fe)-rich phyllosilicates associated with Ca- and Fe-carbonates. The high $pCO_2$ experiment (10 MPa i.e. $CO_2$ = 659.7 mmol.$L^{-1}$) involves the precipitation of magnesite and Fe(Mg)-rich phyllosilicates. All percolated cores contain hematite and reduced carbon. Hereafter, we will discuss the role of $CO_2$ on the hydrothermal alteration of olivine and the fate of carbon in the ultramafic aggregates.

### *4.1. Alteration of olivine and formation of carbonates during low $CO_2$ concentration experiments (6.26 – 62.6 mmol.$L^{-1}$)*

The comparison of experiments SC1-L and SC2-M shows an increase in the mean dissolution rate of olivine with $CO_2$ partial pressure: 1.43 × $10^{-8}$ $s^{-1}$ at $pCO_2$ = 0.1 MPa (sample SC1-L); 6.55 × $10^{-8}$ $s^{-1}$ at $pCO_2$ = 1 MPa (sample SC2-M). These results are consistent with previous studies reporting the effect of $CO_2$ concentration on olivine dissolution rates by controlling the activity of $H^+$ ions in the solution (Rosso and Rimstidt, 2000; Hänchen et al., 2006). $H^+$ ions are assumed to govern the kinetics of olivine dissolution by favoring the protonation of Mg–O and Fe–O bonds (in Mg–O–Si and Fe–O–Si arrangements) to form Mg and Fe complexes associated with silicic acid (Casey and Bunker, 1990; Wogelius and Walther, 1990; Pokrovsky and Schott, 2000). In our study, the dissolution rate of olivine is correlated to the activity of protons in the fluid: it is multiplied by

609 4.6 when the $H^+$ concentration is quadrupled between experiments SC1-L ($H^+$ = 0.04 mmol.$L^{-1}$) and SC2-M ($H^+$ = 0.16 mmol.$L^{-1}$) based on PhreeqC calculations (Parkhurst and Appelo, 2013). However, the outlet concentrations of Si showed that the dissolution rate of olivine evolved differently between these two experiments: it reached rapidly a steady state in experiment SC1-L while it fluctuated throughout experiment SC2-M.

In porous media, the dissolution rate of olivine is controlled by local chemical equilibrium conditions, which are themselves determined by the mass transfer of solutes to reactive sites, the adsorption of such chemical species at the Mg-silicate surface and the residence time of fluids at mineral interfaces (Peuble et al., 2015b). Accordingly, we postulate that the injection of a low concentration of $H^+$ ions in experiment SC1-L ($pCO_2$ = 0.1 MPa) allowed the dissolution rate of olivine to rapidly achieve a steady state at the sample scale, independently of the rock hydrodynamic properties. In experiment SC2-M, $CO_2$ concentrations were 10 times greater ($pCO_2$ = 1 MPa), which increased the difference to equilibrium between olivine and fluids. During this experiment, the olivine dissolution rate never reached a steady state. We speculate that this rate varied locally and temporally along the percolated core depending on local fluid flow conditions and reactive surface areas.

Unlike the dissolution of olivine, the outlet concentrations of Ca and Fe suggest that the precipitation rate of Ca-carbonates and Fe-bearing phases (carbonates and oxides) reached a steady state in both low $pCO_2$ experiments (except for Fe in sample SC1-L). The precipitation of Ca- and Fe- carbonates (i.e. calcite and siderite) appears contradictory with the Mg-rich composition of the initial ultramafic system (olivine $Fo_{90}$). Furthermore, the outlet fluids of low $pCO_2$ experiments do contain magnesium coming from the dissolution of olivine (Fig. 3b), and PhreeqC geochemical simulations indicate that they are supersaturated with respect to magnesite (Parkhurst and Appelo, 2013). These inconsistencies highlight the competitive processes in the precipitation kinetics between Mg-, Ca- and Fe-carbonates, due to the different chemical affinities of $Mg^{2+}$, $Ca^{2+}$ and $Fe^{2+}$ ions with water (e.g., Pokrovsky and Schott, 2002). $Mg^{2+}$ has a highly hydrated character compared to $Ca^{2+}$ and $Fe^{2+}$ (Pokrovsky and Schott, 2002; Schott et al., 2009; Gautier, 2012). Hänchen et al. (2008) observed that the crystallization of magnesite is generally hindered by the intermediate precipitation of hydrous Mg-carbonates (e.g., nesquehonite, hydromagnesite) especially under low $CO_2$ partial pressure conditions (< 0.3 MPa). Hence, the precipitation rate of magnesite can be up to six orders of magnitude slower than that of other carbonates such as calcite (Saldi et al., 2009; Saldi et al., 2012). Because of these thermo-kinetic restrictions, the Mg-rich samples SC1-L and SC2-M promoted the crystallization of calcite and siderite at the expense of magnesite.

This means that the potential for $CO_2$ mineralization in olivine-dominated basements under low $pCO_2$ conditions (0.1 – 1 MPa) is primarily regulated by the amount of iron provided by the mafic silicate and the amount of calcium brought in by the percolating fluids; both mechanisms favoring the precipitation of siderite ± calcite. Magnesium is mainly incorporated into transient, hydrous and amorphous phases (Mg(Fe)-rich (proto-)phyllosilicates) that probably developed from the destabilization of brucite, as it is commonly reported during serpentinization of olivine (Delvigne et al., 1979; Escario et al., 2018; Tutolo et al., 2018). Thus, if we tentatively extrapolate these results to ultramafic reservoirs infiltrated by relatively low $pCO_2$ waters, we can model the hydrothermal alteration of olivine in areas located far from the $CO_2$ input by the following reaction:

$$5\ Mg_{1.80}Fe_{0.20}SiO_4 + CO_2 + 8\ H_2O + 0.01\ CaO_{(aq)} = 8\ Mg(OH_2) + Fe_{0.95}Mg_{0.04}Ca_{0.01}CO_3 + 0.96\ MgO_{(aq)} + 0.05\ FeO_{(aq)} + 5\ SiO_{2(aq)} \quad (3)$$

*Brucite* *Siderite*

Under low $CO_2$ concentrations (here defined as being ≤ 62.6 mmol.$L^{-1}$), the dissolution of five moles of olivine produces eight moles of hydrous minerals (e.g., brucite) but only one mole of Fe-carbonates. Such olivine alteration products (especially brucite) may then induce negative feedback effects on the completion of the reaction (Malvoisin and Brunet, 2014), but also on the hydrodynamic properties of the rock. Indeed, differential pressure measurements revealed a sharp decrease in the permeability of samples SC1-L and SC2-M even though porosity values display little change over time. This suggests that the decrease in permeability is primarily controlled by the structure of secondary minerals (mainly the hydrous phases) clogging fluid pathways in the host rock, in agreement with the results obtained in previous flow-through serpentinization experiments for similar fluid flow conditions (Godard et al., 2013; Peuble et al., 2015b; Farough et al., 2016; Luhmann et al., 2017a).

### *4.2. Alteration of olivine and formation of carbonates during a high $CO_2$ concentration experiment (659.7 mmol.$L^{-1}$)*

High $pCO_2$ experiment SC3-H has probably the highest dissolution rate of olivine, and paradoxically, lower Si outlet fluid concentrations than in experiment SC2-M. The strong dissolution of olivine in sample SC3-H is characterized by abundant etch-pits, similar to those described on several experimental (e.g., Grandstaff, 1978; Malvoisin et al., 2012; King et al.,

2014; Peuble et al., 2015a) and natural samples (Velbel and Ranck, 2008; Velbel, 2009), and attributed to an anisotropic dissolution of the Mg-silicate (King et al., 2014; Peuble et al., 2015a ). The relatively low concentrations of Si in this experiment can be ascribed to the development of large Fe(Mg)-rich phyllosilicates (Fig. 5d), trapping part of the Si released upon olivine dissolution. As for the hydrous minerals of low $pCO_2$ experiments, these phyllosilicates are presumably transitional phases formed before serpentinization. However, their formation appears to be related to the $pCO_2$ since the largest phyllosilicates were observed in sample SC3-H. We postulate that the use of a higher concentration of $CO_2$ in this experiment has facilitated the growth of these phases by increasing the dissolution rate of olivine under lower pH conditions (Wogelius and Walther, 1990; Hänchen et al., 2006; Prigiobbe et al., 2009).

The identified serpentine precursors resemble an iddingsitized form of olivine according to optical, microscopic and Raman observations (Figs. 4-6). Iddingsitization of olivine is an oxidation and hydration reaction leading to the conservation of Si, the loss of Mg (that is leached out from the olivine surfaces) and the gain of Fe (being preferentially converted into ferric iron) in weathered ultramafic rocks (Delvigne et al., 1979). The more prominent serpentine precursors in sample SC3-H (compared to samples SC1-L and SC2-M) have depleted the percolating fluids in Si and Fe relative to Mg suggesting an underestimation of the olivine dissolution rate in sample SC3-H (compared to samples SC1-L and SC2-M). They also promoted the concentration of ferric iron micro-particles (hematite) along dissolved olivine surfaces. These Fe-oxides may then have acted as preferential nuclei for the polymerization of Fe(Mg)-rich phyllosilicates, as it was previously observed during late stages of olivine iddingsitization (Lee et al., 2015).

In sample SC3-H, most of the Mg released upon olivine dissolution was incorporated into a large matrix of magnesite (Fig. 5f). These results confirm that a high concentration of $CO_2$ (659.7 $mmol.L^{-1}$), resulting in a high dissolution rate of olivine and consequently a high concentration of $Mg^{2+}$ in the fluid, is required to overcome the difficulty of Mg-carbonates precipitation (due to the highly hydrated character of $Mg^{2+}$ compared with $Ca^{2+}$ and $Fe^{2+}$ ions - see discussion before). Under these conditions, the main alteration reaction of olivine is dominated by the formation of magnesite according to the following reaction:

$$3\ Mg_{1.80}Fe_{0.20}SiO_4 + CO_2 + 0.07\ CaO_{(aq)} = Mg_{0.91}Ca_{0.07}Fe_{0.02}CO_3 + 0.58\ FeO_{(aq)} + 4.49\ MgO_{(aq)} + 3\ SiO_{2(aq)} \quad (4)$$

*Magnesite*

The comparison of reactions (3) and (4) shows that, for every mole of $CO_2$ converted into carbonates, five moles of olivine need to be dissolved in the low $pCO_2$ experiments but only three in the high $pCO_2$ experiment. This demonstrates a greater potential of olivine to trap $CO_2$ as carbonates when the inlet fluid has a higher partial pressure of $CO_2$.

Magnesite is associated with Fe(Mg)-rich phyllosilicates in sample SC3-H. However, the outlet concentration values of Mg, Fe and Ca indicate that these two secondary minerals precipitated at different times in the ultramafic core. The sharp decrease in Fe outlet concentrations coupled with the increasing release of Mg in the first hours of injection suggest an almost immediate polymerization of serpentine fibrous precursors. This process then slowed down after 84 hours, with the increase in Fe outlet concentrations up to ≈ 0.19 ppm. At $t \approx 45$h, magnesite began to crystallize by first incorporating calcium, then magnesium and iron, resulting in a significant decrease in the outlet concentrations of Ca, Mg and Fe after $t \approx$ 45, 71 and 116 hours, respectively. These concentrations stabilized after 135 hours, indicating that the olivine carbonation rate rapidly reached a steady state in the percolated aggregate.

The onset of the stable carbonation of olivine is correlated with a linear decrease in permeability after 135 hours in sample SC3-H. As in low $pCO_2$ experiments, this correlation attests to negative feedback effects of some olivine alteration products on rock flow paths by reducing pore hydraulic radius and increasing pore tortuosity over time. However, the porosity of sample SC3-H increased throughout the injection whatever the scenarios considered (Fig. 10c). These results suggest first that the overall decrease in rock pore volume during magnesite and serpentine precursors precipitation is (at least temporarily and locally) offset by the porosity created upon olivine dissolution, maintaining fluid renewal at reaction front interfaces (Peuble et al., 2017). They also show that the decrease in permeability recorded during experiment SC3-H is not controlled by the crystallization of secondary minerals. The decrease in permeability is most likely attributed to the heterogeneous distribution of these secondary minerals in the percolated core, which affects primarily the major fluid pathways.

### *4.3. Oxidation of olivine ferrous iron and the fate of carbon*

The characterization of reacted samples revealed the presence of reduced carbon, trapping from 0.04% (sample SC3-H) to 0.17% (sample SC2-M) of the $CO_2$ injected into the percolated olivine aggregates (Fig. 8 and Table 3). To our knowledge, it is the first time that

reduced carbon was measured after olivine alteration experiments in presence of $CO_2$-bearing fluids although it is observed in oceanic and ophiolitic serpentinites (Ménez et al., 2012; Galvez et al., 2013; Sforna et al., 2018), sometimes in association to carbonates (Schwarzenbach et al., 2016). Also, it is worth to note that the precipitation of reduced carbon has been previously reported after another set of reactive percolation experiments using a different set-up and flow-bench (Luquot et al., 2012). These reactive percolation experiments consisted in injecting of $CO_2$-bearing brines ($pCO_2$ = 6 MPa; $CO_2$ = 402 mmol.$L^{-1}$) into chlorite/zeolite-rich sandstones at T=95 °C and P=10 MPa. They produced reduced carbon grains with the same poorly organized crystallographic structure as those observed in our samples. Luquot et al. (2012) proposed that these carbon grains were formed after concomitant reduction of the injected $CO_2$ in association to the oxidation of ferrous iron in chlorite. The oxidation of iron liberates electrons (Eq. 5), inducing locally a more reduced environment, which in turn would favor carbon reduction (Eq. 6).

$$Fe^{2+} = Fe^{3+} + e^- \quad (5)$$

$$CO_2 + 4H^+ + 4\,e^- = C^0 + 2H_2O \quad (6)$$

The oxidation of $Fe^{2+}$ during serpentinization is often associated to the abiotic generation of $H_2$ produced from $H_2O$ reduction. Subsequently, $H_2$ can react with $CO_2$ to form a wide range of reduced carbon species including condensed carbonaceous matter (Galvez et al., 2013; Martinez et al., 2017; Sforna et al., 2018) and possibly methane (McCollom, 2016). Some studies have shown that the production of reduced carbon-bearing phases may be kinetically favored in serpentinizing ultramafic systems when metal alloys are present (Horita and Berndt, 1999; Fu et al., 2008; Lazar et al., 2012) because they act as catalysts. Accordingly, we can question the fact that the sintered nickel porous disk positionned upstream of the olivine sample can have acted similarly during our experiments thus favoring the formation of reduced carbon phases albeit, to our knowledge, Ni-Fe alloys have been shown to act as catalysts of the methane production only (Horita and Berndt, 1999). Alternatively, Milesi et al. (2016) recently demonstrated on the basis of thermodynamical calculations that solid carbonaceous material can be formed during serpentinization without catalysts. Furthermore, they showed that the compositions of fluids sampled in ultramafic-hosted hydrothermal vents were consistent with an equilibrium between $CO_{2(aq)}$ and some condensed carbon phases, thus suggesting that these reactions are probably of major importance in ultramafic basements along oceanic spreading centers.

During our experiments, the presence of hematite and iddingsite at the olivine surface indicates that oxidation of ferrous iron did occur at the fluid/mineral interface. The pH and pE

of the inlet fluids were calculated using the PhreeqC geochemical code (Parkhurst and Appelo, 2013); pH values of 4.5, 3.9 and 3.4 and pE values of 5.4, 6.5 and 7.3 were estimated for experiments SC1-L, SC2-M and SC3-H, respectively. When reported on a pE-pH stability diagram of Fe- and C-species, hematite is thermodynamically stable for the conditions characterizing the inlet fluid, which is consistent with a reaction of $Fe^{2+}$ oxidation at the sample inlet (Figure 11a, b, and c). This oxidation reaction is probably balanced by the reduction of $CO_2$ into carbon, promoting a strong decrease in the fluid pE down to -2.6, -1.4 and -0.3 in experiments SC1-L, SC2-M and SC3-H, respectively. So, assuming that pH stays low and constant (e.g., at the onset of the reaction or close to the $CO_2$ injection point), carbon reduction could be favored over water reduction (and hydrogen production) (Figure 11d, e, and f), in contrast to what is classically suggested in the literature to balance the oxidation of ferrous iron during serpentinization (Klein et al., 2009). However, the field of stability of carbon is very narrow and olivine dissolution will increase the pH of reacting fluids downstream, consuming $H^+$ ions in the solutions (Pokrovsky and Schott, 2000; Escario et al., 2018). The observation of carbonates in samples SC1-L, SC2-M and SC3-H suggests an increase of the fluid pH to at least values of 6.3, 5.4 and 4.8, respectively. The precipitation of hydrous phases (Fe(Mg)-rich phyllosilicates) requires an increase of pH to at least values of 6.6 in experiments SC1-L – SC2-M and of 7.5 in experiment SC3-H (Fig. 11a-c). This two-step mechanism (redox reactions followed by dissolution-precipitation reactions), by which reactions along flow paths are controlled by feedback processes between the dissolution of olivine and the changes in fluid composition (including pH), could explain both the limited distribution of reduced carbon, observed only in the pores close to the inlet (Fig. 8), and the predominance of carbonate and hydrous phases in the reacted samples. It is worth noticing that carbonate (magnesite) precipitation conditions are favored in the high $pCO_2$ experiment (minimum pE-pH variations), which could explain the observed high carbonation efficiency in sample SC3-H.

Thermodynamic modeling suggests that carbon reduction is strongly controlled by the low pH of fluids, a condition that is rarely met in natural carbonate bearing serpentinizing ultramafic basements, which are dominated by alkaline fluids (Ludwig et al., 2006; Chavagnac et al., 2013; Milesi et al., 2016). This process should however be taken into account when predicting the fate of carbon in the case of a $CO_2$-injection experiment in an ultramafic basement.

## 5. Summary and conclusions

This experimental study explores the role of $CO_2$ and fluid flow on the hydrothermal alteration of olivine. Results provide new information to characterize the fluid-rock reactions in the case of an ultramafic aquifer pervaded by $CO_2$-rich hydrothermal waters. It is the first step to improve the parameterization of future numerical models specifically by allowing the measurement of macroscopic characteristics of the mass transfer mechanisms resulting from complex coupled flow-reaction pore scale processes.

Far from the $CO_2$ input i.e. under low $pCO_2$ conditions (from 0.1 to 1 MPa), olivine will be mainly altered into hematite and Mg(Fe)-rich phyllosilicates. These iddingsitic-type assemblages may clog most of the rock flow paths, resulting in a strong decrease in permeability in a few days. Some carbonates can form in these conditions, but they are mainly composed of calcium and iron despite the initial Mg-rich system ($Fo_{90}$). This denotes less favorable conditions of crystallization for Mg- than for Ca- and Fe-carbonates.

Closer to the $CO_2$ input (i.e. $pCO_2$ = 10 MPa), olivine will be more efficiently altered. This causes the formation of abundant etch-pits on the olivine surfaces and a larger amount of poorly crystallized Fe(Mg)-rich phyllosilicates depleting the percolating fluids in Si and Fe relative to Mg. In addition to these hydrous phases, magnesite precipitates as dense clusters in the large pores. The carbonation rate of olivine can be 3 to 11 times higher at a $pCO_2$ of 10 MPa than when $pCO_2$ is 10 to 100 times lower, respectively. Both carbonated and hydrous minerals induce apparently little changes in porosity but a strong decrease in permeability, attesting to negative feedback effects of the olivine alteration products on the fluid flow.

Despite the differences in secondary mineralogy between the low and high $pCO_2$ experiments, all samples contain reduced carbon that may indicate a competition for reduction and carbonation processes; both participating to the mineral sequestration of $CO_2$. Carbon formation suggests reducing conditions probably caused by the oxidation of ferrous iron into ferric iron. For the specific boundary condition of the experiments, carbon deposits are limited to the pores located at the inlet in relation to the low production of hematite and the pH gradient in the samples. Nevertheless, one can speculate that the formation of carbon can be a significant mechanism of $CO_2$ sequestration in olivine-dominated basements.

For industrial application, long lasting injection is required. Accordingly, the objective should be to prevent as best as possible precipitation in the vicinity of the well and to favor mineralization as far as possible from the injection well. When investigating the injection of a reactive fluid from a well, the most important feature is that seepage velocity decreases linearly to quadratically as the distance to injection increases and therefore the apparent (or

847 dynamic) water/rock ratio decreases rapidly. Consequently, the most important feature for
848 optimizing injection is to inject at the largest flow rate as possible in order to locate
849 mineralization as far as possible from the injection well and thus mitigate permeability
850 reduction effects. From this perspective, one can speculate from the permeability (Fig. 2) and
851 $CO_2$ trapping (Fig. 10) curves that the medium $pCO_2$ value (1 MPa) would be the most
852 favorable option.
853
854 **Acknowledgements**

855 This research was supported by the ANR (CO2FIX-ANR-08-PCO2-003-02) and Université
856 Montpellier 2 (Programme-Pluridisciplinaire-Energie). We thank C. Nevado and D. Delmas
857 for the preparation of the polished sections, and C. Douchet for analytical assistance during
858 ICP-MS analyses at the AETE-ISO ("Analyses des Eléments en Trace dans l'Environnement
859 et ISOtopes") platform from the OREME observatory (University of Montpellier). We also
860 thank Benjamin M. Tutolo and two anonymous reviewers for their detailed comments and
861 suggestions and Rajdeep Dasgupta for editorial handing
862
863
864 **Table captions**
865
866 Table 1. Experimental setup and sample characteristics for the three experiments.
867
868 Table 2. Concentrations of major elements (Si, Mg, Fe and Ca, in ppm) measured in the inlet
869 fluid by ICP-MS.
870
871 Table 3. Bulk rock analyses. Hydrogen and carbon contents recalculated as $H_2O$ and $CO_2$
872 contents respectively in the initial powder and the percolated olivine cores SC2-M and SC3-H
873 (analytical blanks subtracted).
874
875 Table 4. Mass balance calculations. Estimates of dissolved olivine and precipitated secondary
876 minerals relative to the initial samples mass, and corresponding changes in rock porosity.
877
878 **Figure captions**
879
880 Figure 1. Diagram of the ICARE-RFTS3 experimental device (Geosciences Montpellier).

Figure 2. Samples permeability $k$ (in $10^{-15}$ m²) as a function of time (in hours) during experiments SC1-L ($pCO_2$ = 0.1 MPa; $CO_2$ = 6.26 mmol.L$^{-1}$), SC2-M ($pCO_2$ = 1 MPa; $CO_2$ = 62.6 mmol.L$^{-1}$) and SC3-H ($pCO_2$ = 10 MPa; $CO_2$ = 659.7 mmol.L$^{-1}$). Symbols in inset.

Figure 3. (a) Si, (b) Mg, (c) Fe and (d) Ca outlet fluid concentrations (in ppm) versus the elapsed time of the experiments (in hours). Dotted lines correspond to the inlet fluid composition. Symbols in inset.

Figure 4. Binocular microscope photography of the olivine aggregates (a) before and (b,c,d) after the percolation experiments: (b) sample SC1-L ($pCO_2$ = 0.1 MPa; $CO_2$ = 6.26 mmol.L$^{-1}$), (c) sample SC2-M ($pCO_2$ = 1 MPa; $CO_2$ = 62.6 mmol.L$^{-1}$) and (d) sample SC3-H ($pCO_2$ = 10 MPa; $CO_2$ = 659.7 mmol.L$^{-1}$). White arrows denote the fluid flow direction during the experiments. The white square indicates the location of the SEM image displayed in Figure 8.

Figure 5. SEM images of the samples after the experiments (a,b) SC1-L ($pCO_2$ = 0.1 MPa; $CO_2$ = 6.26 mmol.L$^{-1}$), (c) SC2-M ($pCO_2$ = 1 MPa; $CO_2$ = 62.6 mmol.L$^{-1}$) and (d,e,f) SC3-H ($pCO_2$ = 10 MPa; $CO_2$ = 659.7 mmol.L$^{-1}$). Reacted samples are mainly composed of olivine. (a,b,c) Formation of amorphous Mg(Fe)-rich phyllosilicates (phyll) associated with micrograins of silica, calcite and siderite. (d) Precipitation of poorly crystallized Fe(Mg)-rich phyllosilicates forming a loose network of curled fibers. (e) Strong dissolution of olivine evidenced by the development of conical-shaped etch-pits. (f) Sample SC3-H is also characterized by the formation of dense clusters of magnesite (mgn) in large pores located near dissolved olivine grains.

Figure 6. Raman analyses performed in the inlet area (< 5 mm) of the three percolated samples. Raman spectra of forsterite, hematite, lizardite and iddingsite are from Cnopnras et al. (1991), De Faria et al. (1997), Auzende et al. (2004), and Kuebler et al. (2003), respectively.

Figure 7. Raman spectrum of the percolated sample SC3-H ($pCO_2$ = 10 MPa; $CO_2$ = 659.7 mmol.L$^{-1}$). The standard spectrum of magnesite is shown for comparison (Rividi et al., 2010).

Figure 8. (a, b) SEM images showing organic carbon in pores located at the inlet (< 5 mm). in sample SC2-M ($pCO_2$ = 1 MPa; $CO_2$ = 62.6 mmol.$L^{-1}$). (c) Raman spectrum obtained on the corresponding area with the typical D and G bands of reduced carbon at respective values of 1310 and 1560 $cm^{-1}$ (Galvez et al., 2013).

Figure 9. Room temperature Mössbauer spectra performed on (a) the initial bulk rock and the reacted powders of (b) sample SC1-L ($pCO_2$ = 0.1 MPa; $CO_2$ = 6.26 mmol.$L^{-1}$), (c) sample SC2-M ($pCO_2$ = 1 MPa; $CO_2$ = 62.6 mmol.$L^{-1}$) and (d) sample SC3-H ($pCO_2$ = 10 MPa; $CO_2$ = 659.7 mmol.$L^{-1}$). The experimental data are represented with circles, the fitted components with dotted light and dark grey lines. Symbols in inset.

Figure 10: Mass (a) of dissolved olivine and (b) $CO_2$ trapped as carbon and carbonates normalized to the initial samples mass. $CO_2$ contents deduced from geochemical analyses are also reported. (c) Changes in porosity induced by the alteration of olivine into carbonates (siderite or calcite in samples SC1-L and SC2-M; magnesite in sample SC3-H) and hydrous phases (brucite or lizardite in samples SC1-L and SC2-M; goethite or lizardite in sample SC3-H) in relation to the initial samples porosity. See text for details. Symbols in inset.

Figure 11: pH-pE stability diagram of (a, b, c) iron and (d, e, f) carbon phases . Calculations are made at 185 °C under the $CO_2$ concentration conditions of (a, d) experiment SC1-L ($CO_2$ = 6.26 mmol.$L^{-1}$), (b, e) experiment SC2-M ($CO_2$ = 62.6 mmol.$L^{-1}$) and (c, f) experiment SC3-H ($CO_2$ = 659.7 mmol.$L^{-1}$) using the JCHESS geochemical code (Van Der Lee and De Windt, 2001). Crosses represent the initial pE and pH conditions of the fluid in each experiment according to the calculations made with the PhreeqC geochemical code (Parkhurst and Appelo, 2013). Initial pE values were calculated assuming an electric potential of -0.3 for a Volvic® water at 25 °C and 0.1 MPa (Lorne et al., 1999). Abbreviations: mgt: magnetite; Fe-phyll: Fe-rich phyllosilicates, sid: siderite.

## References

Andreani, M., Luquot, L., Gouze, P., Godard, M., Hoise, E., Gibert, B., 2009. Experimental study of carbon sequestration reactions controlled by the percolation of $CO_2$-rich brine through peridotites. Environmental Science & Technology 43, 1226-1231.

948 Andreani, M., Mevel, C., Boullier, A.M., Escartin, J., 2007. Dynamic control on serpentine
949 crystallization in veins: constraints on hydration processes in oceanic peridotites.
950 Geochemistry Geophysics Geosystems 8, 1-24.
951 Andreani, M., Munoz, M., Marcaillou, C., Delacour, A., 2013. μXANES study of iron redox
952 state in serpentine during oceanic serpentinization. Lithos 178, 70-83.
953 Audier, M., Oberlin, A., Oberlin, M., Coulon, M., Bonnetain, L., 1981. Morphology and
954 crystalline order in catalytic carbons. Carbon 19, 217-224.
955 Auzende, A.-L., Daniel, I., Reynard, B., Lemaire, C., Guyot, F., 2004. High-pressure
956 behaviour of serpentine minerals: a Raman spectroscopic study. Physics and Chemistry of
957 Minerals 31, 269-277.
958 Bearat, H., McKelvy, M.J., Chizmeshya, A.V.G., Gormley, D., Nunuez, R., Carpenter, R.W.,
959 Squires, K., Wolf, G.H., 2006. Carbon sequestration via aqueous olivine mineral carbonation:
960 role of passivating layer formation. Environmental Science & Technology 40, 4802-4808.
961 Bernoulli, D., Weissert, H., 1985. Sedimentary fabrics in Alpine ophicalcites, south Pennine
962 Arosa zone, Switzerland. Geology 13, 755-758.
963 Beyssac, O., Goffe, B., Petitet, J.-P., Froigneux, E., Moreau, M., Rouzaud, J.-N., 2003. On the
964 characterization of disordered and heterogeneous carbonaceous materials by Raman
965 spectroscopy. Spectrochimica Acta Part A 59, 2267-2276.
966 Casey, W.H., Bunker, B., 1990. Leaching of mineral and glass surfaces during dissolution.
967 Reviews in mineralogy and geochemistry 23, 397-426.
968 Chavagnac, V., Monnin, C., Ceuleneer, G., Boulart, C., Hoareau, G., 2013. Characterization
969 of hyperalkaline fluids produced by low‐temperature serpentinization of mantle peridotites
970 in the Oman and Ligurian ophiolites. Geochemistry, Geophysics, Geosystems 14, 2496-2522.
971 Cnopnras, A., 1991. Single crystal Raman spectra of forsterite, fayalite, and monticellite.
972 American Mineralogist 76, 110L1109.
973 Coggon, R.M., Teagle, D.A.H., Smith-Duque, C.E., Alt, J.C., Cooper, M.J., 2010.
974 Reconstructing past seawater Mg/Ca and Sr/Ca from mid-ocean ridge flank calcium carbonate
975 veins. Science 327, 1114-1117.
976 Dasgupta, R., Hirschmann, M.M., 2010. The deep carbon cycle and melting in Earth's
977 interior. Earth and Planetary Science Letters 298, 1-13.
978 Daval, D., Hellmann, R., Saldi, G.D., Wirth, R., Knauss, K.G., 2013. Linking nm-scale
979 measurements of the anisotropy of silicate surface reactivity to macroscopic dissolution rate
980 laws: New insights based on diopside. Geochimica et Cosmochimica Acta 107, 121-134.

Daval, D., Sissmann, O., Menguy, N., Saldi, G.D., Guyot, F., Martinez, I., Corvisier, J., Garcia, B., Machouk, I., Knauss, K.G., Hellmann, R., 2011. Influence of amorphous silica layer formation on the dissolution rate of olivine at 90°C and elevated $pCO_2$. Chemical Geology 284, 193-209.

De Faria, D.L.A., Venâncio Silva, S., De Oliveira, M.T., 1997. Raman microspectroscopy of some iron oxides and oxyhydroxides. Journal of Raman spectroscopy 28, 873-878.

Deer, W.A., Howie, R.A., Zussman, J., 1992. An introduction to the rock-forming minerals. Longman Scientific & Technical Hong Kong.

Delvigne, J., Bisdom, E.B.A., Sleeman, J., Stoops, G., 1979. Olivines, their pseudomorphs and secondary products. Stiboka.

Dullien, F.A.L., 1979. Porous media: fluid transport and pore structure. Academic press, New-York.

Dyar, M.D., Agresti, D.G., Schaefer, M.W., Grant, C.A., Sklute, E.C., 2006. Mössbauer Spectroscopy of Earth and Planetary Materials. Annual Review of Earth and Planetary Sciences 34, 83-125.

Escario, S., Godard, M., Gouze, P., Leprovost, R., 2018. Experimental study of the effects of solute transport on reaction paths during incipient serpentinization. Lithos.

Farough, A., Moore, D.E., Lockner, D.A., Lowell, R.P., 2016. Evolution of fracture permeability of ultramafic rocks undergoing serpentinization at hydrothermal conditions: An experimental study. Geochemistry, Geophysics, Geosystems 17, 44-55.

Ferry, J.M., 2000. Patterns of mineral occurrence in metamorphic rocks. American Mineralogist 85, 1573-1588.

Fu, Q., Foustoukos, D.I., Seyfried, W.E., 2008. Mineral catalyzed organic synthesis in hydrothermal systems: An experimental study using time-of-flight secondary ion mass spectrometry. Geophysical research letters 35.

Galvez, M.E., Beyssac, O., Martinez, I., Benzerara, K., Chaduteau, C., Malvoisin, B., Malavieille, J., 2013. Graphite formation by carbonate reduction during subduction. Nature Geoscience 6, 473-477.

Gautier, Q., 2012. Cinétiques de précipitation de minéraux carbonatés magnésiens, influence de ligands organiques et conséquences pour la séquestration minérale du CO2. Université Paris-Est.

Giammar, D.E., Bruant, J.R.G., Peters, C.A., 2005. Forsterite dissolution and magnesite precipitation at conditions relevant for deep saline aquifer storage and sequestration of carbon dioxide. Chemical Geology 217, 257-276.

1015 Gislason, S.R., Wolff-Boenisch, D., Stefansson, A., Oelkers, E., Gunnlaugsson, E.,
1016 Sigurdardottir, H., Sigfusson, B., Broecker, W., Matter, J., Stute, M., Axelsson, G.,
1017 Fridriksson, T., 2010. Mineral sequestration of carbon dioxide in basalt: the CarbFix project.
1018 International Journal of Greenhouse Gas Control 4, 537–545.
1019 Godard, M., Luquot, L., Andreani, M., Gouze, P., 2013. Incipient hydration of mantle
1020 lithosphere at ridges: a reactive-percolation experiment. Earth and Planetary Science Letters
1021 371, 92-102.
1022 Grandstaff, D.E., 1978. Changes in surface area and morphology and the mechanism of a
1023 forsterite dissolution. Geochimica et Cosmochimica Acta 42, 1899-1901.
1024 Hänchen, M., Prigiobbe, V., Baciocchi, R., Mazzotti, M., 2008. Precipitation in the Mg-
1025 carbonate system: effects of temperature and $CO_2$ pressure. Chemical Engineering Science 63,
1026 1012-1028.
1027 Hänchen, M., Prigiobbe, V., Storti, G., Seward, T.M., Mazzoti, M., 2006. Dissolution kinetics
1028 of fosteritic olivine at 90–150°C including effects of the presence of $CO_2$. Geochimica et
1029 Cosmochimica Acta 70, 4403-4416.
1030 Hansen, L.D., Dipple, G.M., Gordon, T.M., Kellett, D.A., 2005. Carbonated serpentinite
1031 (listwanite) at Atlin, British Columbia: A geological analogue to carbon dioxide sequestration.
1032 The Canadian Mineralogist 43, 225-239.
1033 Horita, J., Berndt, M.E., 1999. Abiogenic methane formation and isotopic fractionation under
1034 hydrothermal conditions. Science 285, 1055-1057.
1035 Jamtveit, B., Malthe-Sørenssen, A., Kostenko, O., 2008. Reaction enhanced permeability
1036 during retrogressive metamorphism. Earth and Planetary Science Letters 267, 620-627.
1037 Javoy, M., Pineau, F., 1991. The volatiles record of a popping rock from the Mid-Atlantic
1038 ridge at 14°N: chemical and isotopic composition of gas trapped in the vesicles. Earth and
1039 Planetary Science Letters 107, 598-611.
1040 Jun, Y.-S., Giammar, D.E., Werth, C.J., 2013. Impacts of geochemical reactions on geologic
1041 carbon sequestration. Environmental Science & Technology 47, 3-8.
1042 Kelemen, P.B., Hirth, G., 2012. Reaction-driven cracking during retrograde metamorphism:
1043 Olivine hydration and carbonation. Earth and Planetary Science Letters 345, 81-89.
1044 Kelemen, P.B., Manning, C.E., 2015. Reevaluating carbon fluxes in subduction zones, what
1045 goes down, mostly comes up. Proceedings of the National Academy of Sciences 112, E3997-
1046 E4006.
1047 Kelemen, P.B., Matter, J., 2008. In situ carbonation of peridotite for $CO_2$ storage. Proceedings
1048 of the National Academy of Sciences 105, 17295–17300.

1049 Kelemen, P.B., Matter, J., Streit, E.E., Rudge, J.F., Curry, W.B., Blusztajn, J., 2011. Rates
1050 and mechanisms of mineral carbonation in peridotite: natural processes and recipes for
1051 enhanced, in situ $CO_2$ capture and storage. Annual Review of Earth and Planetary Sciences
1052 39, 546-576.
1053 King, H.E., Satoh, H., Tsukamoto, K., Putnis, A., 2014. Surface-specific measurements of
1054 olivine dissolution by phase-shift interferometry. American Mineralogist 99, 377-386.
1055 Klein, F., Bach, W., Jöns, N., McCollom, T., Moskowitz, B., Berquó, T., 2009. Iron
1056 partitioning and hydrogen generation during serpentinization of abyssal peridotites from 15°N
1057 on the Mid-Atlantic Ridge. Geochimica et Cosmochimica Acta 73, 6868-6893.
1058 Klein, F., McCollom, T.M., 2013. From serpentinization to carbonation: New insights from a
1059 $CO_2$ injection experiment. Earth and Planetary Science Letters 379, 137-145.
1060 Kuebler, K., 2009. A comparison of iddingsite alteration in two terrestrial basalts and the
1061 ALHA 77005 martian meteorite using Raman spectroscopy and electron microprobe analyses.
1062 Kuebler, K., 2013. A comparison of the iddingsite alteration products in two terrestrial basalts
1063 and the Allan Hills 77005 martian meteorite using Raman spectroscopy and electron
1064 microprobe analyses. Journal of Geophysical Research: Planets (1991–2012) 118, 803-830.
1065 Kuebler, K., Wang, A., Haskin, L.A., Jolliff, B.L., 2003. A study of olivine alteration to
1066 iddingsite using Raman spectroscopy, Lunar and Planetary Institute Science Conference
1067 Abstracts, p. 1953.
1068 Lazar, C., McCollom, T., Manning, C.E., 2012. Abiogenic methanogenesis during
1069 experimental komatiite serpentinization: implications for the evolution of the early
1070 Precambrian atmosphere. Chemical Geology 326, 102-112.
1071 Lee, M.R., Tomkinson, T., Hallis, L.J., Mark, D.F., 2015. Formation of iddingsite veins in the
1072 martian crust by centripetal replacement of olivine: Evidence from the nakhlite meteorite
1073 Lafayette. Geochimica et Cosmochimica Acta 154, 49-65.
1074 Lorne, B., Perrier, F., Avouac, J.-P., 1999. Streaming potential measurements: 1. Properties of
1075 the electrical double layer from crushed rock samples. Journal of Geophysical Research: Solid
1076 Earth (1978–2012) 104, 17857-17877.
1077 Ludwig, K.A., Kelley, D.S., Butterfield, D.A., Nelson, B.K., Früh-Green, G.L., 2006.
1078 Formation and evolution of carbonate chimneys at the Lost City Hydrothermal Field.
1079 Geochimica et Cosmochimica Acta 70, 3625-3645.
1080 Luhmann, A.J., Tutolo, B.M., Bagley, B.C., Mildner, D.F., Scheuermann, P.P., Feinberg,
1081 J.M., Ignatyev, K., Seyfried Jr, W., 2017a. Chemical and physical changes during seawater

flow through intact dunite cores: An experimental study at 150–200° C. Geochimica et Cosmochimica Acta 214, 86-114.

Luhmann, A.J., Tutolo, B.M., Tan, C., Moskowitz, B.M., Saar, M.O., Seyfried, W.E., 2017b. Whole rock basalt alteration from $CO_2$-rich brine during flow-through experiments at 150 ° C and 150 bar. Chemical Geology 453, 92-110.

Luquot, L., Andreani, M., Gouze, P., Camps, P., 2012. $CO_2$ percolation experiment through chlorite/zeolite-rich sandstone (Pretty-Hill Formation – Otway Basin–Australia). Chemical Geology 294-29, 75-88.

Malvoisin, B., Brunet, F., 2014. Water diffusion-transport in a synthetic dunite: Consequences for oceanic peridotite serpentinization. Earth and Planetary Science Letters 403, 263-272.

Malvoisin, B., Brunet, F., Carlut, J., Rouméjon, S., Cannat, M., 2012. Serpentinization of oceanic peridotites: 2. Kinetics and processes of San Carlos olivine hydrothermal alteration. Journal of Geophysical Research 117.

Mao, S., Duan, Z., 2009. The viscosity of aqueous alkali-chloride solutions up to 623 K, 1000 bar and high ionic strength. International Journal of Thermophysics 30, 1510-1523.

Martinez, I., Vacquand, C., Kularatne, K., Sissmann, O., Milesi, V., Bernard, S., 2017. Formation of reduced carbon compounds using natural catalysts in hydrothermal experiments, Goldschmidt Abstract, 2602.

Matter, J.M., Kelemen, P.B., 2009. Permanent storage of carbon dioxide in geological reservoirs by mineral carbonation. Nature Geoscience 2, 837-841.

McCollom, T.M., 2016. Abiotic methane formation during experimental serpentinization of olivine. Proceedings of the National Academy of Sciences 113, 13965-13970.

McGrail, B.P., Spane, F.A., Sullivan, E.C., Bacon, D.H., Hund, G., 2011. The Wallula basalt sequestration pilot project. Energy Procedia 4, 5653-5660.

Ménez, B., Pasini, V., Brunelli, D., 2012. Life in the hydrated suboceanic mantle. Nature Geoscience 5, 133-137.

Milesi, V., McCollom, T.M., Guyot, F., 2016. Thermodynamic constraints on the formation of condensed carbon from serpentinization fluids. Geochimica et Cosmochimica Acta 189, 391-403.

Nakamura, K., Kato, Y., 2004. Carbonatization of oceanic crust by the seafloor hydrothermal activity and its significance as a $CO_2$ sink in the early Archean. Geochimica et Cosmochimica Acta 68, 4595-4618.

Nasir, S., Sayigh, A., Razak, A., Al Harthy, A., Al-Khirbash, S., Al-Jaaidi, O., Musllam, A., Al-Mishwat, A., Al-Bu'saidi, S., 2007. Mineralogical and geochemical characterization of listwaenite from the Semail ophiolite, Oman. Chemie Der Erde-Geochemistry 67, 213-228.

Noël, J., Godard, M., Oliot, E., Martinez, I., Williams, M., Boudier, F., Rodriguez, O., Chaduteau, C., Escario, S., Gouze, P., 2018. Evidence of polygenetic carbon trapping in the Oman Ophiolite: Petro-structural, geochemical, and carbon and oxygen isotope study of the Wadi Dima harzburgite-hosted carbonates (Wadi Tayin massif, Sultanate of Oman). Lithos.

Oelkers, E.H., Gislason, S.R., Matter, J., 2008. Mineral carbonation of $CO_2$. Elements 4, 333-337.

Parkhurst, D.L., Appelo, C.A.J., 2013. Description of Input and Examples for PHREEQC Version 3--a Computer Program for Speciation, Batch-reaction, One-dimensional Transport, and Inverse Geochemical Calculations: Ch. A43. U.S. Geological Survey Techniques and Methods book 6. USGS.

Paterson, M.S., 1990. Rock deformation experimentation. Geophysical monograph series 56, 187-194.

Peuble, S., Andreani, M., Godard, M., Gouze, P., Barou, F., Van De Moortèle, B., Mainprice, D., Reynard, B., 2015a. Carbonate mineralization in percolated olivine aggregates: Linking effects of crystallographic orientation and fluid flow. American Mineralogist 100, 474-482.

Peuble, S., Andreani, M., Gouze, P., Pollet-Villard, M., Reynard, B., Van de Moortele, B., 2017. Multi-scale characterization of the incipient carbonation of peridotite. Chemical Geology 476, 150-160.

Peuble, S., Godard, M., Luquot, L., Andreani, M., Martinez, I., Gouze, P., 2015b. $CO_2$ geological storage in olivine rich basaltic aquifers: New Insights from flow-through experiments. Applied Geochemistry 52, 174-190.

Pineau, F., Javoy, M., 1994. Strong degassing at ridge crests: the behaviour of dissolved carbon and water in basalt glasses at 14°N, Mid-Atlantic ridge. Earth and Planetary Science Letters 123, 179-184.

Pokrovsky, O.S., Schott, J., 2000. Kinetics and mechanism of forsterite dissolution at 25°C and pH from 1 to 12. Geochimica et Cosmochimica Acta 64, 3313–3325.

Pokrovsky, O.S., Schott, J., 2002. Surface chemistry and dissolution kinetics of divalent metal carbonates. Environmental Science & Technology 36, 426-432.

Prigiobbe, V., Costa, G., Baciocchi, R., Hänchen, M., Mazzotti, M., 2009. The effect of $CO_2$ and salinity on olivine dissolution kinetics at 120°C. Chemical Engineering Science 64, 3510-3515.

1148 Rausch, S., Böhm, F., Bach, W., Klügel, A., Eisenhauer, A., 2013. Calcium carbonate veins in
1149 ocean crust record a threefold increase of seawater Mg/Ca in the past 30 million years. Earth
1150 and Planetary Science Letters 362, 215-224.
1151 Rividi, N., Van Zuilen, M., Philippot, P., Menez, B., Godard, G., Poidatz, E., 2010.
1152 Calibration of carbonate composition using micro-Raman analysis: application to planetary
1153 surface exploration. Astrobiology 10, 293-309.
1154 Rosso, J.J., Rimstidt, J.D., 2000. A high resolution study of forsterite dissolution rates.
1155 Geochimica et Cosmochimica Acta 64, 797-811.
1156 Rudge, J.F., Kelemen, P.B., Spiegelman, M., 2010. A simple model of reaction-induced
1157 cracking applied to serpentinization and carbonation of peridotite. Earth and Planetary
1158 Science Letters 291, 215-227.
1159 Saldi, G., Schott, J., Pokrobsky, O., Gautier, Q., Oelkers, E., 2012. An experimental study of
1160 magnesite precipitation rates at neutral to alkaline conditions and 100-200°C as a function of
1161 pH, aqueous solution composition and chemical affinity. Geochimica et Cosmochimica Acta
1162 83, 93-109.
1163 Saldi, G.D., Jordan, G., Schott, J., Oelkers, E.H., 2009. Magnesite growth rates as a function
1164 of temperature and saturation state. Geochimica et Cosmochimica Acta 73, 5646-5657.
1165 Schott, J., Pokrovsky, O.S., Oelkers, E.H., 2009. The link between mineral
1166 dissolution/precipitation kinetics and solution chemistry. Reviews in Mineralogy &
1167 Geochemistry 70, 207-258.
1168 Schwarzenbach, E.M., Früh-Green, G.L., Bernasconi, S.M., Alt, J.C., Plas, A., 2013.
1169 Serpentinization and carbon sequestration: A study of two ancient peridotite-hosted
1170 hydrothermal systems. Chemical Geology 351, 115-133.
1171 Schwarzenbach, E.M., Gill, B.C., Gazel, E., Madrigal, P., 2016. Sulfur and carbon
1172 geochemistry of the Santa Elena peridotites: Comparing oceanic and continental processes
1173 during peridotite alteration. Lithos 252, 92-108.
1174 Seifritz, W., 1990. $CO_2$ disposal by means of silicates. Nature 345, 486.
1175 Sforna, M.C., Brunelli, D., Pisapia, C., Pasini, V., Malferrari, D., Ménez, B., 2018. Abiotic
1176 formation of condensed carbonaceous matter in the hydrating oceanic crust. Nature
1177 Communications 9, 5049.
1178 Sissmann, O., Brunet, F., Martinez, I., Guyot, F., Verlaguet, A., Pinquier, Y., Daval, D., 2014.
1179 Enhanced olivine carbonation within a basalt as compared to single-phase experiments:
1180 reevaluating the potential of $CO_2$ mineral sequestration. Environmental Science &
1181 Technology.

Steefel, C.I., DePaolo, D.J., Lichtner, P.C., 2005. Reactive transport modeling: an essential tool and a new research approach for the Earth sciences. Earth and Planetary Science Letters 240, 539-558.

Tutolo, B.M., Luhmann, A.J., Tosca, N.J., Seyfried, W.E., 2018. Serpentinization as a reactive transport process: The brucite silicification reaction. Earth and Planetary Science Letters 484, 385-395.

Van Der Lee, J., De Windt, L., 2001. Present state and future directions of modeling of geochemistry in hydrogeological systems. Journal of Contaminant Hydrology 47, 265-282.

Van der Lee, J., De Windt, L., Lagneau, V., Goblet, P., 2003. Module-oriented modeling of reactive transport with HYTEC. Computers and Geosciences 29, 265–275.

Velbel, M.A., 2009. Dissolution of olivine during natural weathering. Geochimica et Cosmochimica Acta 73, 6098-6113.

Velbel, M.A., Ranck, J.M., 2008. Etch pits on naturally altered olivine from dunites of the Appalachian Blue Ridge Mountains, North Carolina, USA. Mineralogical Magazine 72, 145-148.

Wogelius, R.A., Walther, J.V., 1990. Olivine dissolution at 25°C: effects of pH, $CO_2$, and organic acids. Geochimica et Cosmochimica Acta 55, 943-954.

Yeghicheyan, D., Bossy, C., Coz, M.B., Douchet, C., Granier, G., Heimburger, A., Lacan, F., Lanzanova, A., Rousseau, T., Seidel, J.-L., 2013. A compilation of Silicon, Rare Earth Element and twenty-one other Trace Element concentrations in the Natural River Water Reference Material SLRS-5 (NRC-CNRC). Geostandards and Geoanalytical Research.

Zeebe, R.E., Caldeira, K., 2008. Close mass balance of long-term carbon fluxes from ice-core $CO_2$ and ocean chemistry records. Nature Geoscience 1, 312-315.

**Table**

| Experimental conditions (T = 185°C) | | | |
|---|---|---|---|
| Experiments | SC1-L | SC2-M | SC3-H |
| Duration of experiments (hours) | 92.88 | 156.36 | 333.34 |
| Total pressure (MPa) | 25.0 | 25.0 | 20.0 |
| $CO_2$ partial pressure (MPa) | 0.1 | 1.0 | 10.0 |
| $CO_2$ (mmol.$L^{-1}$) | 6.26 | 62.6 | 659.7 |
| Initial magnetic susceptibility ($10^{-8}$ $m^3$.$Kg^{-1}$) | 16.9 | 17.6 | 19.2 |
| Final magnetic susceptibility ($10^{-8}$ $m^3$.$Kg^{-1}$) | 16.9 | 17.4 | 21.8 |
| Initial porosity (%) | 10.96 | 11.30 | 10.57 |
| Initial permeability ($10^{-15}$ $m^2$) | 1.876 | 1.561 | 4.589 |
| Final permeability ($10^{-15}$ $m^2$) | 0.075 | 0.019 | 0.005 |

Table 1
Peuble et al., 2018

| ICP-MS data | Det. Limit | Injected fluid |
|---|---|---|
| Si (ppm) | 0.815 | 14.95 |
| Mg | 0.001 | 8.73 |
| Fe | 0.005 | 0.01 |
| Ca | 0.012 | 12.1 |

Table 2
Peuble et al., 2018

| Bulk rock analyses (wt.%) | Initial olivine powder | SC2-M | SC3-H |
|---|---|---|---|
| $H_2O$ | 0.04 | 0.08 | n.a. |
| $CO_2$ inorganic | < 0.05 | 0.10 | 1.31 |
| $CO_2$ organic* | < 0.05 | 0.17 | 0.04 |
| $CO_2$ total | < 0.05 | 0.27 | 1.35 |

*Note. n.a.: not analyzed ; *organic carbon recalculated as $CO_2$*

Table 3
Peuble et al., 2018

| Mass balance calculations | | SC1-L | SC2-M | SC3-H |
|---|---|---|---|---|
| Mass Variation. $\Delta m/m_0$ in % | Dissolved olivine | -0.48 | -3.69 | -4.31 |
| | Hydrous phases | 0.40 | 3.15 | 0.50 |
| | Carbonates | 0.08 | 0.58 | 3.12 |
| | Carbon | 0.01 | 0.10 | 0.01 |
| | Total | 0.01 | 0.14 | -0.68 |
| | $H_2O$ | 0.18 | 1.44 | 0.10 |
| | $CO_2$ inorganic | 0.03 | 0.22 | 1.61 |
| | $CO_2$ organic* | 0.04 | 0.38 | 0.05 |
| | $CO_2$ total | 0.07 | 0.60 | 1.66 |
| Porosity changes. $\phi/\phi_0$ | Calcite & Brucite | 0.99 | 0.88 | - |
| | Calcite & Serpentine | 0.99 | 0.91 | - |
| | Siderite & Brucite | 0.99 | 0.89 | - |
| | Siderite & Serpentine | 0.99 | 0.93 | - |
| | Magnesite & Goethite | - | - | 1.05 |
| | Magnesite & Serpentine | - | - | 1.03 |

*Note: (-) loss & (+) gain ; *organic carbon recalculated as $CO_2$*

Table 4
Peuble et al., 2018

**Figure**

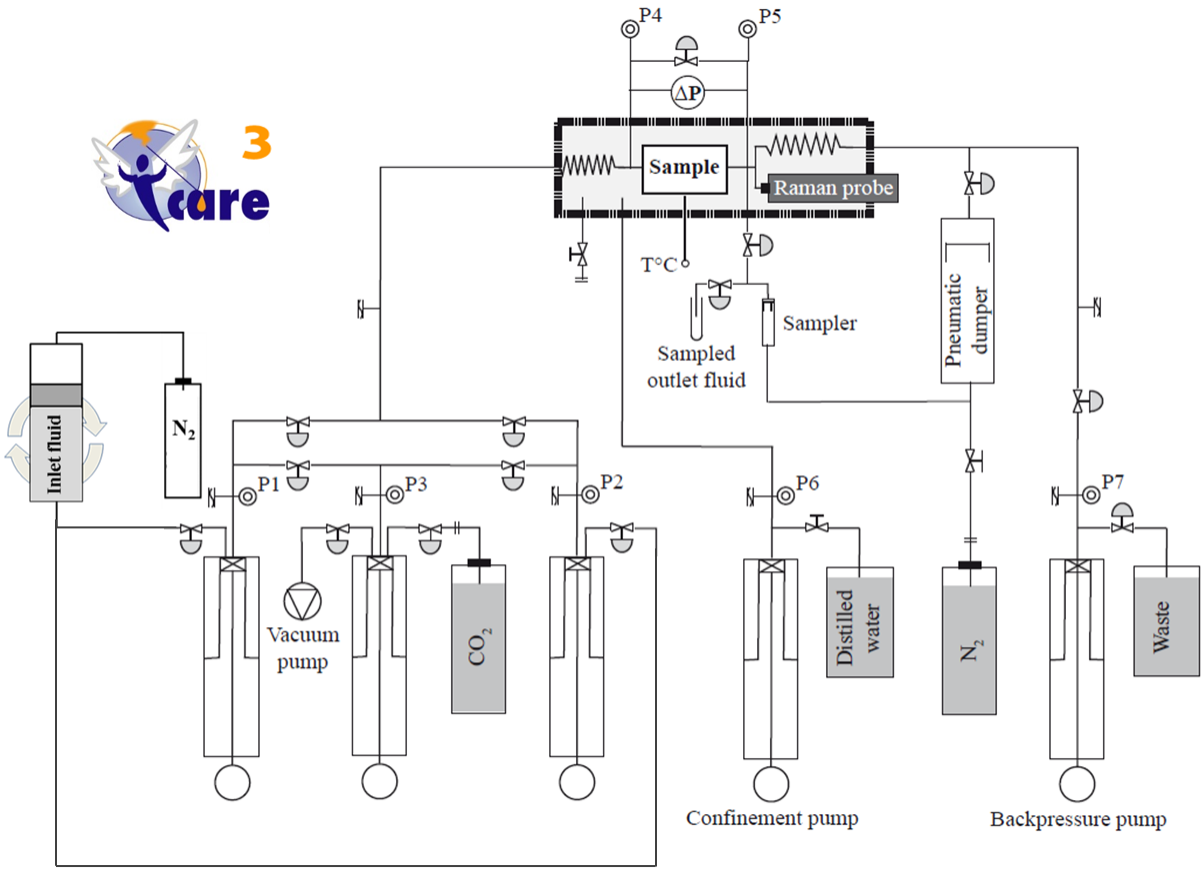


Figure 1. Peuble et al. 2018

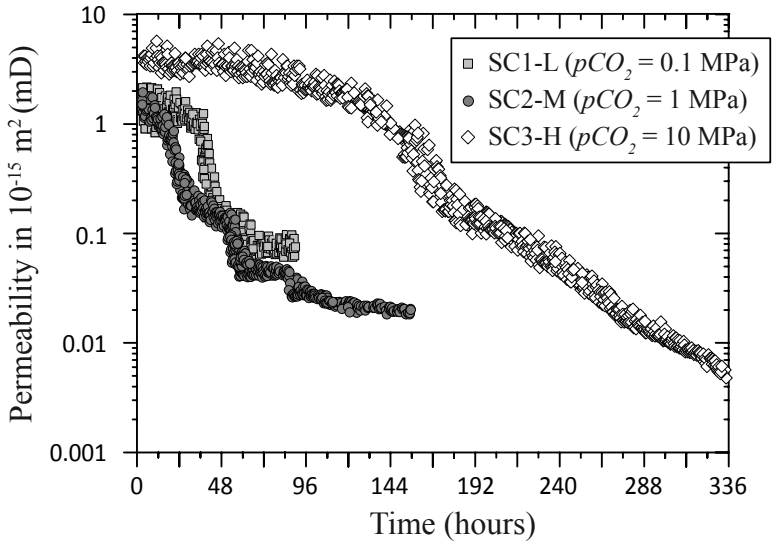


Figure 2. Peuble et al. 2018

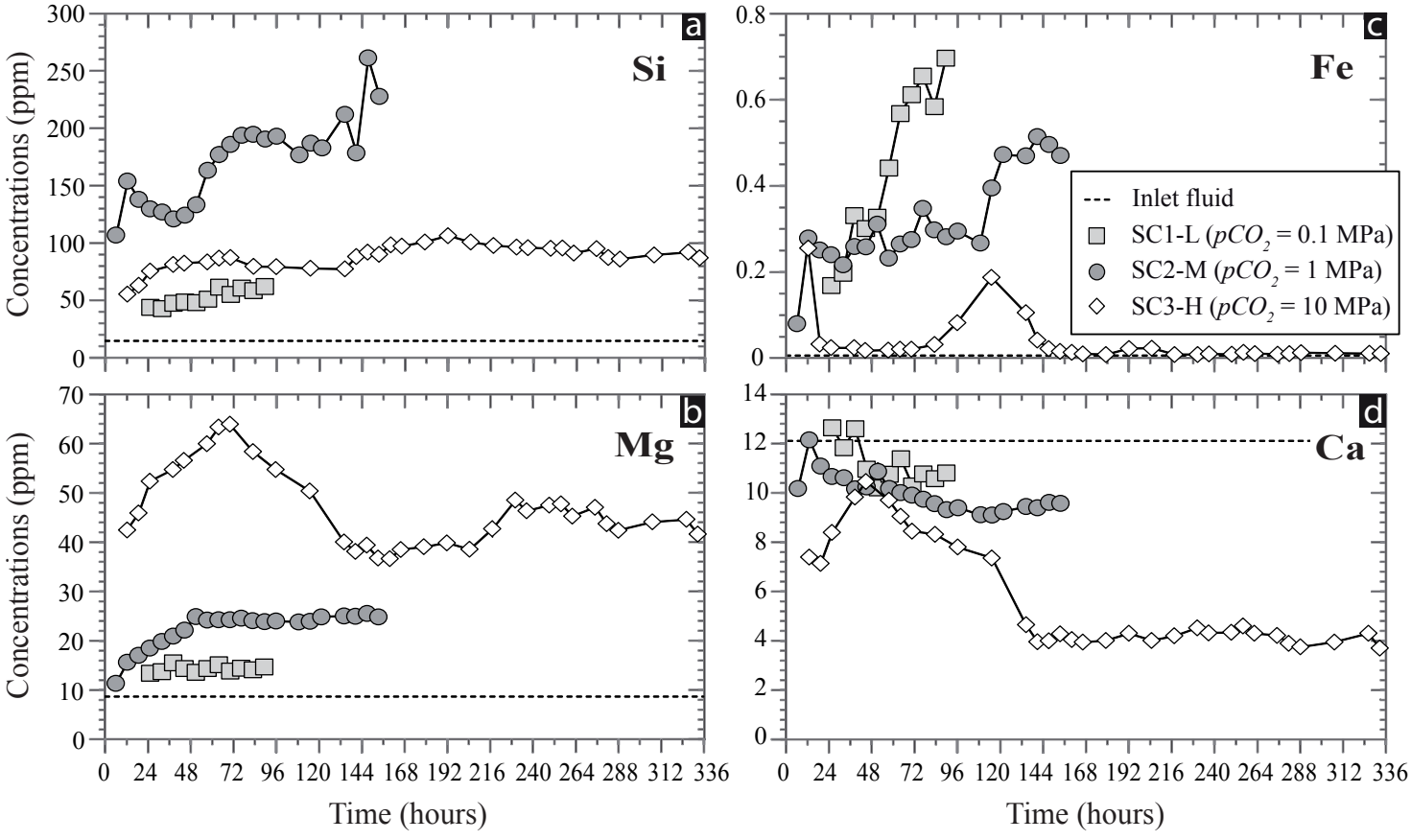


Figure 3. Peuble et al. 2018

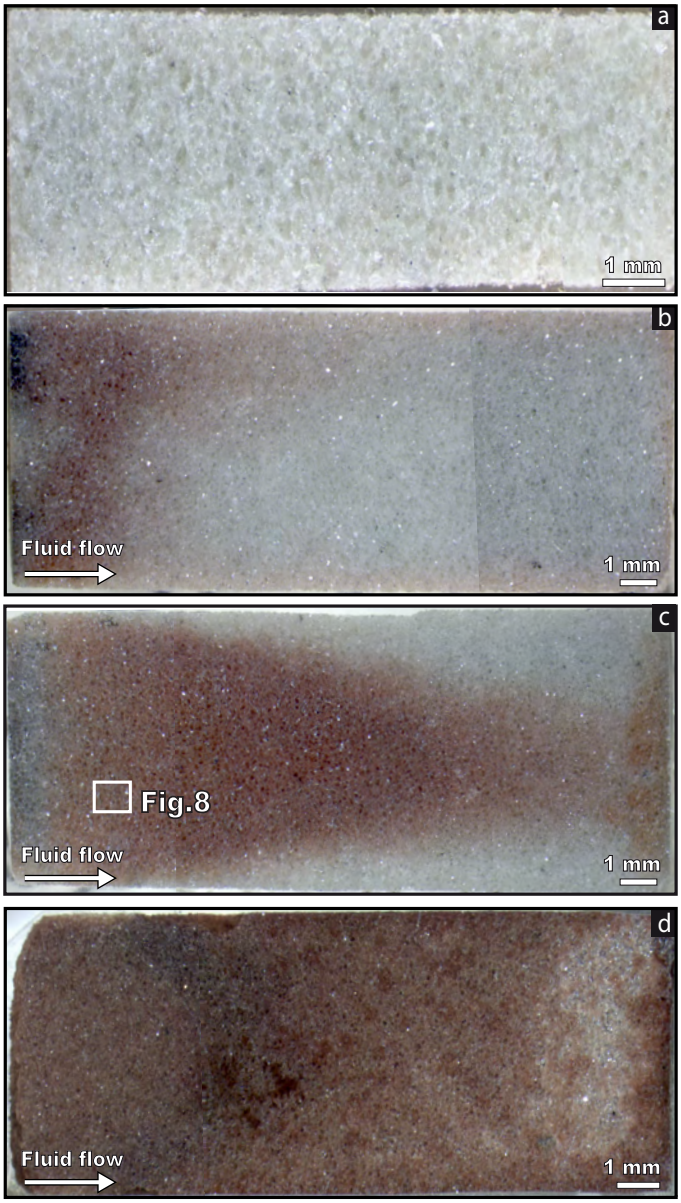


Figure 4. Peuble et al. 2018

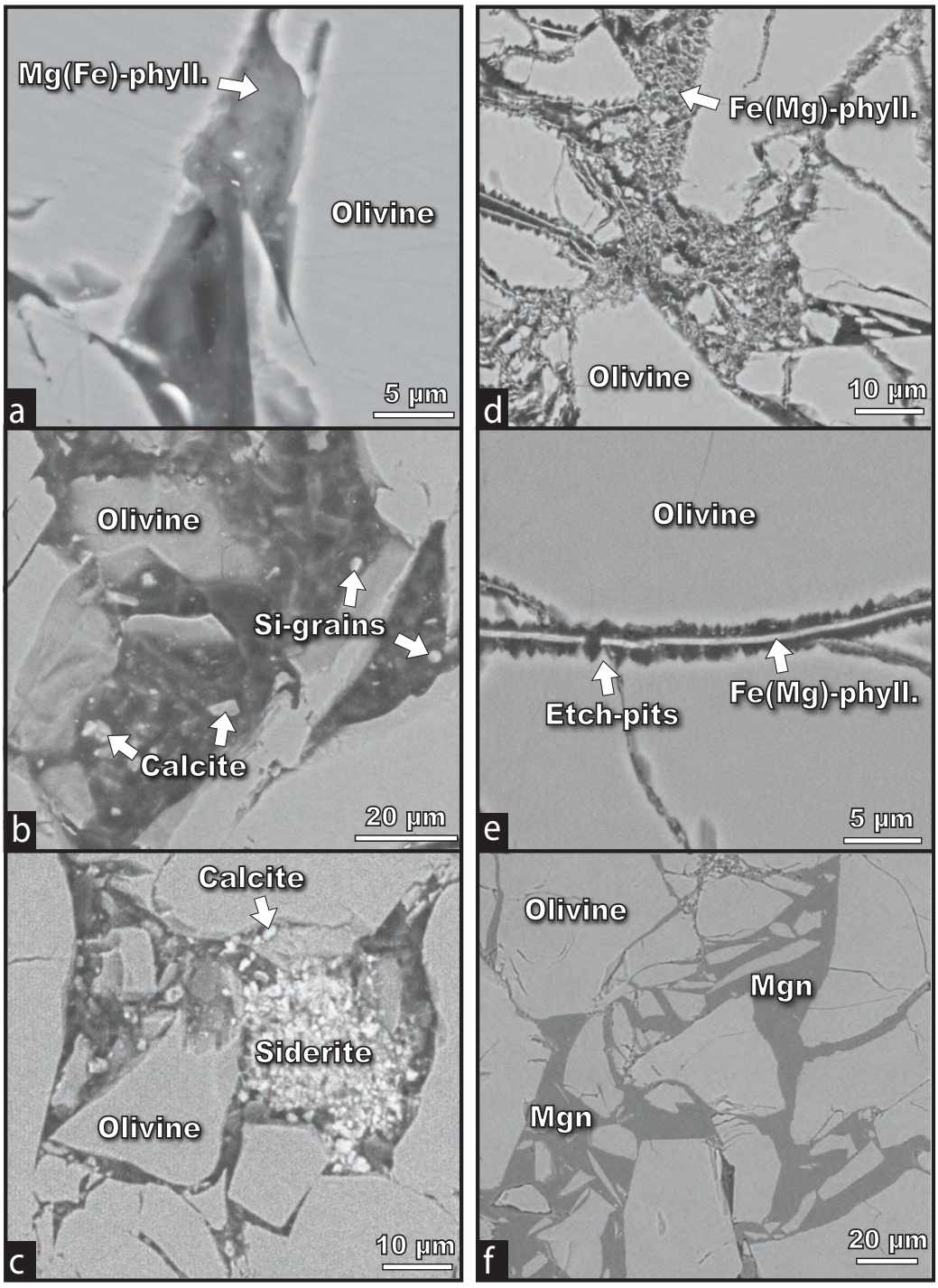


Figure 5. Peuble et al. 2018

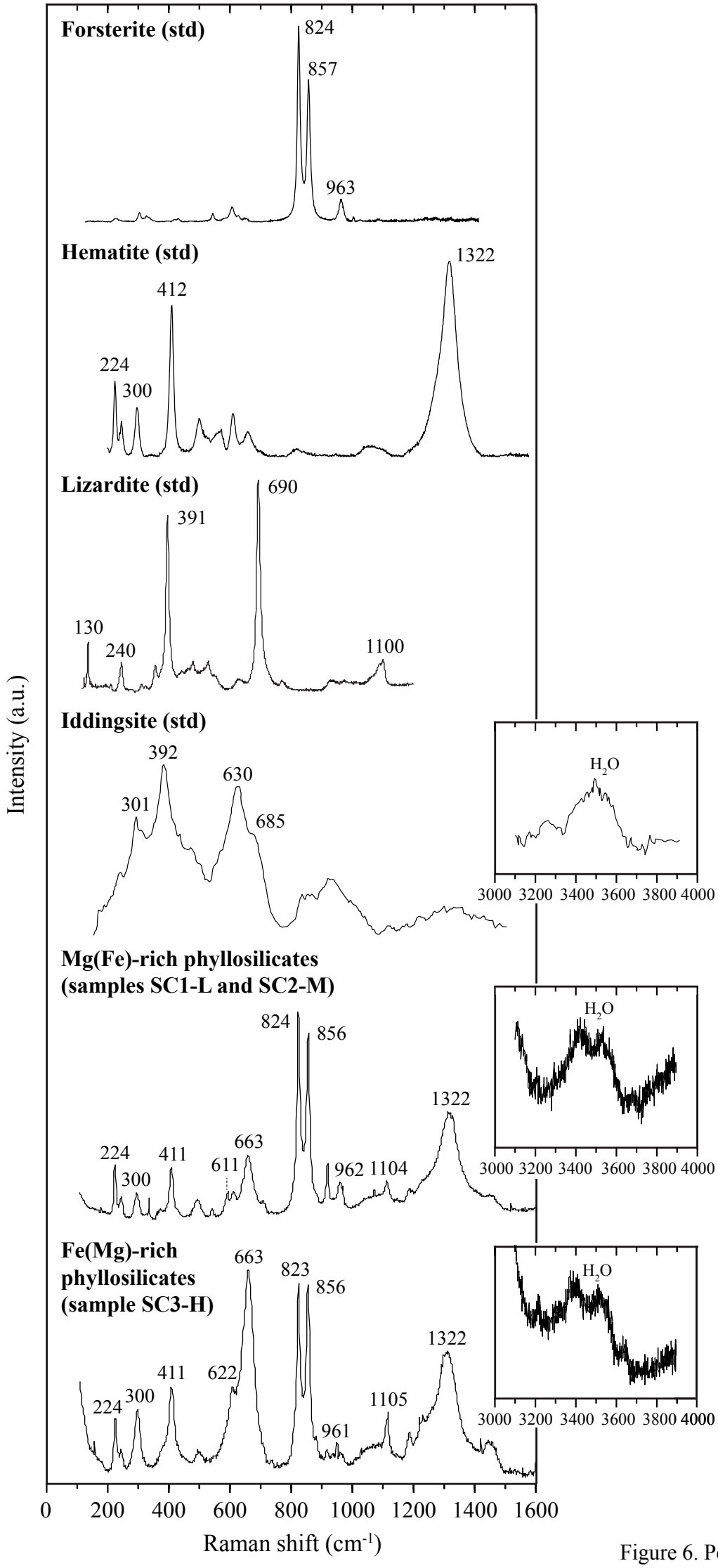


Figure 6. Peuble et al. 2018

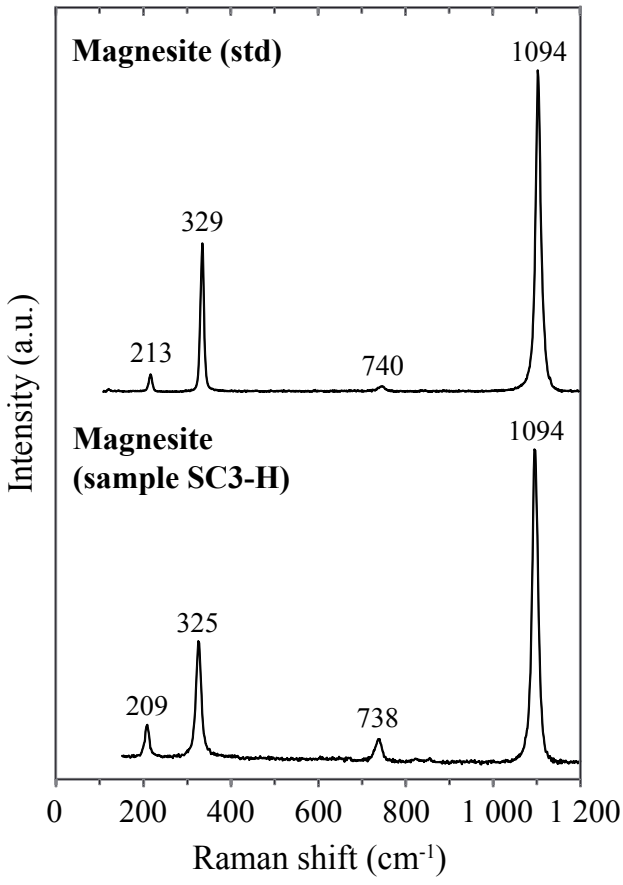


Figure 7. Peuble et al. 2018

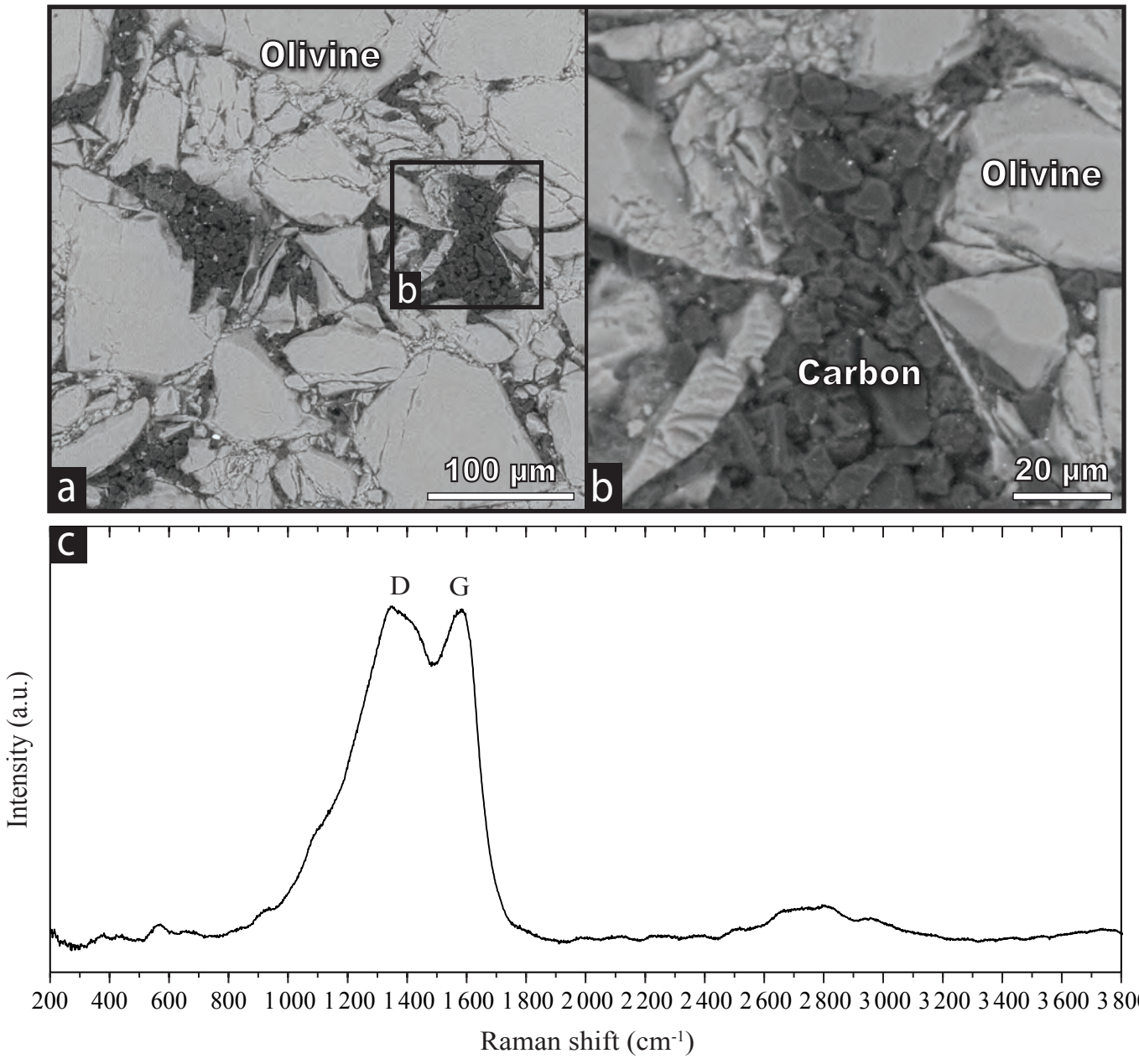


Figure 8. Peuble et al. 2018

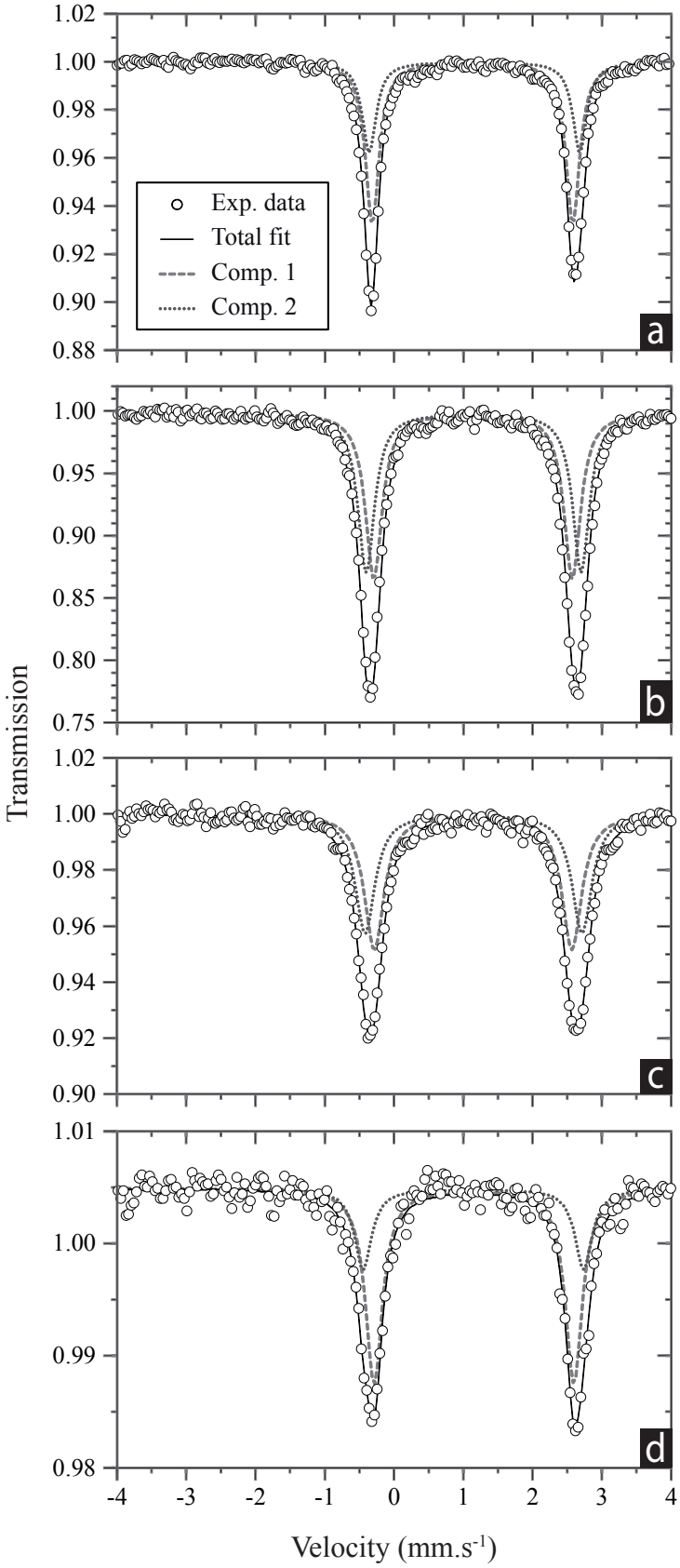


Figure 9. Peuble et al. 2018

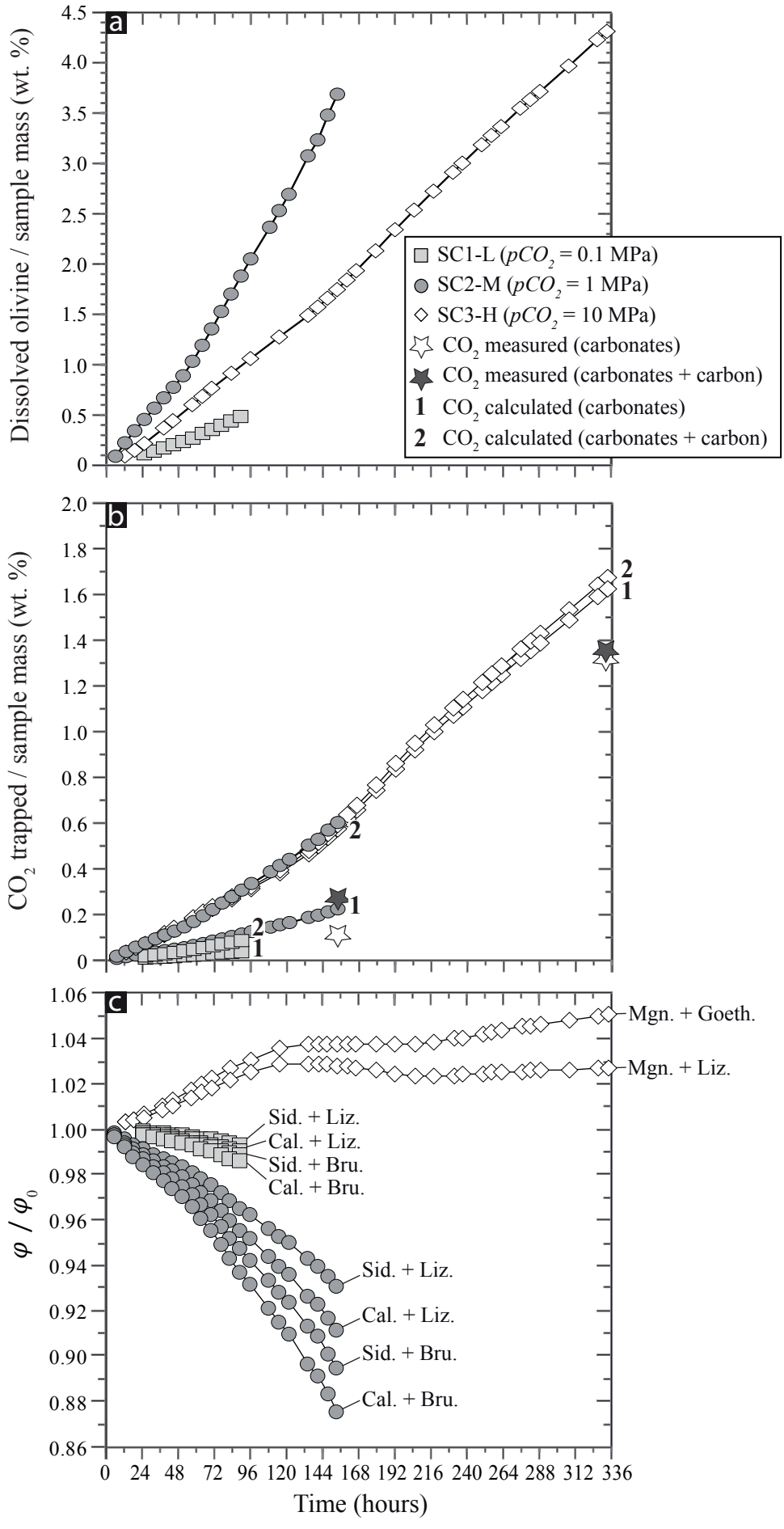


Figure 10. Peuble et al. 2018

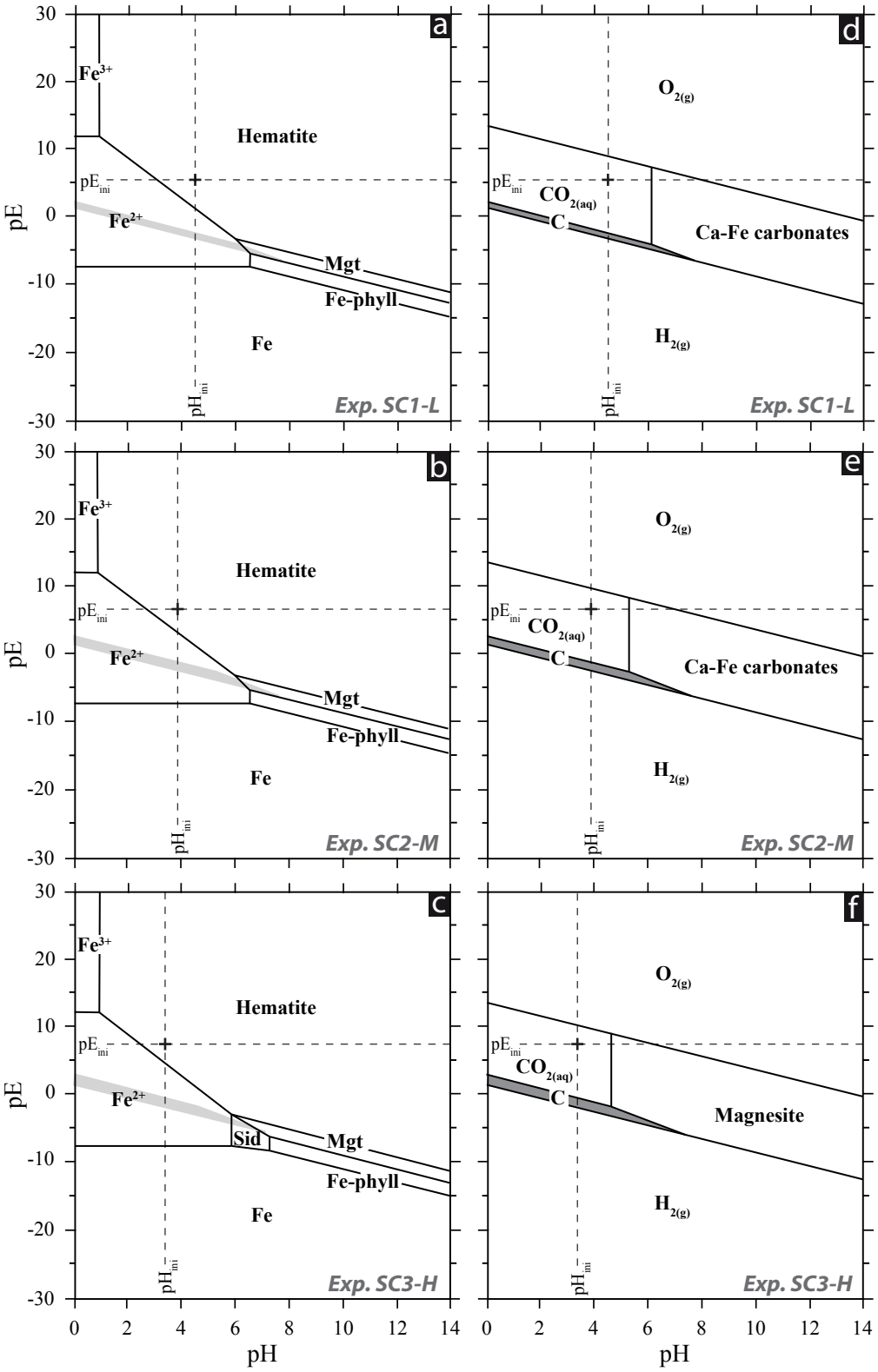


Figure 11. Peuble et al. 2018